

Electronic and magnetic phase diagrams of Kitaev quantum spin liquid candidate $\text{Na}_2\text{Co}_2\text{TeO}_6$

Shengzhi Zhang,^{1,*} Sangyun Lee,² Andrew J. Woods,² Sean M. Thomas,² Roman Movshovich,² Eric Brosha,³ Qing Huang,⁴ Haidong Zhou,⁴ Vivien S. Zapf,^{1,†} and Minseong Lee^{1,‡}

¹*National High Magnetic Field Laboratory, Los Alamos National Laboratory, Los Alamos, NM 87545, USA.*

²*MPA-Q, Los Alamos National Laboratory, Los Alamos, New Mexico 87545, USA.*

³*Los Alamos National Laboratory, Los Alamos, NM 87545, USA.*

⁴*Department of Physics, University of Tennessee, Knoxville, TN 37996, USA.*

(Dated: December 8, 2022)

Recently $3d^7$ Co^{2+} -based magnets with strong spin-orbit coupling effects have been proposed to show dominant Kitaev magnetic exchange interactions and a suppression of Heisenberg interactions. This makes them good candidates to observe Kitaev quantum spin liquid behavior on honeycomb lattices. Here we present physical properties and the phase diagram of a prominent Co^{2+} -based Kitaev quantum spin liquid candidate $\text{Na}_2\text{Co}_2\text{TeO}_6$ for magnetic fields along the a , a^* and c -axis. We measured magnetization, specific heat, dielectric constant, thermal expansion, and magnetocaloric effect to 14 T for most measurements and 60 T for the magnetization along the a^* - and the c -axis. At zero field we find no electric polarization, which is more consistent with a zig-zag antiferromagnetic state than a 3Q model that was proposed. In applied fields sharp features in the dielectric constant indicate the involvement of electric dipoles strongly coupled to magnetism that locally break spatial inversion symmetry, though without net electric polarization. We observe three successive field-induced phase transitions *before* saturation is reached for fields along a and a^* , and two new temperature-induced phase boundaries in the spin-polarized phase. The lowest-field boundary is strongly hysteretic whereas the others are all second-order-like. The highest-field phase boundary has a mean field-like dome shape in temperature-field space. Above the highest-field phase transition at 9.5 T for fields along a , a^* , the magnetocaloric effect shows a drop in spin entropy continuing up at least 20 T, consistent with a spin gap opening. Above 9.5 T the magnetization vs magnetic field approaches saturation, though subject to an additional linear Van-Vleck-like contribution continuing to at least 60 T. A Kitaev quantum spin liquid phases have been suggested between the second and third field-induced phase boundary, or possibly between the third phase boundary and saturation. These phase boundaries participate apparent tricritical points in the phase diagram that should not be allowed for 2nd order phase transitions. Finally, when $H \parallel c$, we observed three critical temperatures in zero magnetic field at and below the antiferromagnetic transition temperature. With increasing magnetic field, the intermediate critical temperature splits into two. Two field induced magnetic transitions appear at 9 T and 15.5 T that are both largely independent of temperature.

I. INTRODUCTION

When magnetism forms on antiferromagnetic honeycomb lattices, the resulting magnetic order is not frustrated when the dominant exchange interaction is isotropic. However, when the exchange interactions are dominated by Kitaev interactions, strong magnetic frustration results and the intriguing Kitaev quantum spin liquid (KQSL) is predicted to form as the ground state [1]. The Kitaev exchange interaction is of the form $K_\gamma S_i^\gamma S_j^\gamma$ where $\gamma \in x, y, z$ indicates the three types of bonds in a honeycomb lattice along the three mutually orthogonal directions.

KQSLs are of particular interest to the quantum computing community. This is because they host quasiparticles that are non-abelian anyons [1]. Non-abelian anyons change the observable state of the system if they are

braided (moved around each other). The resulting braid operations have been shown to be consistent with fully fault-tolerant quantum computation, since the braided state is non-local and topologically protected and thus, inherently resists local errors in the spin configurations [1, 2]. However, the discovery of KQSLs in real magnets is still a significant challenge. Most real KQSL candidates show both Kitaev and Heisenberg interactions, and thus order at zero magnetic field (see below). Luckily, it has been predicted that in applied magnetic fields the long-range order can be suppressed in favor of a KQSL state.

The Kitaev spin Hamiltonian can be materialized in physical systems when $j_{\text{eff}} = \frac{1}{2}$ doublet forms under a strong spin-orbit coupling while crystal field and the conventional Heisenberg type exchange interactions are suppressed due to quantum interference between multiple paths across ligand ions on edge-sharing octahedra [3].

Due to the need for strong spin-orbit coupling, most research on potential KQSLs has focused on the heavier $4d$ and $5d$ ions with the low-spin d^5 electron configuration such as Ru^{3+} and Ir^{4+} . The first prominent candidates were honeycomb iridium oxides $A_2\text{IrO}_3$ with $A = \text{Na}, \text{Li}$ [4], which have recently been extended to in-

* shengzhi@lanl.gov

† vzapf@lanl.gov

‡ ml10k@lanl.gov

clude $A_3\text{LiIr}_2\text{O}_6$ with $A = \text{Ag}$ and H [5, 6]. All of these candidates except for $\text{H}_3\text{LiIr}_2\text{O}_6$ show magnetic ordering at zero magnetic field while $\text{Ag}_3\text{LiIr}_2\text{O}_6$ was shown to form magnetic ordering in cleaner crystals [7, 8] and may show a KQSL in applied magnetic fields. Another highly promising candidate is $\alpha\text{-RuCl}_3$ [9]. It exhibits continuum spin excitations in neutron scattering experiments [10] around the Brillouin zone center, which signifies spinon excitations possibly from Majorana excitations. Moreover, albeit seemingly dependent on growth techniques and the precise stacking structure, a potential half-quantized thermal Hall conductivity suggests a chiral quantum spin liquid phase stabilized by magnetic fields [11–15].

More recently, it has been proposed that certain 3d transition metals, which were previously dismissed by the conventional wisdom that 3d transition metal have small spin-orbit coupling, can also host the Kitaev exchange interactions [16–18]. We note that as long as the spin-orbit coupling is comparable to or larger than the exchange and orbital-lattice interactions, the Kitaev interaction can still dominate. Indeed, $d^7 \text{Co}^{2+}$ with the high spin configuration $t_{2g}^5 e_g^2$ has been shown to provide a strongly spin-orbit coupled pseudospin 1/2 degree of freedom with Kitaev interactions [16–18] given that the crystal field is weak enough that it does not affect the spin-orbit coupling. In $3d^7$ systems, the Kitaev interaction comes almost entirely from the $t_{2g}\text{-}e_g$ hopping process. It is calculated to dominate over the Heisenberg interactions because the $e_g\text{-}e_g$ Heisenberg and off-diagonal exchange interactions cancel those from the $t_{2g}\text{-}e_g$ hopping process [18]. In addition, the more localized nature of 3d orbital than that of 4d and 5d helps suppress second- and third nearest neighbor exchange interactions which make the analysis of data from 4d and 5d compounds much more complicated [16–18].

$\text{Na}_2\text{Co}_2\text{TeO}_6$ has been proposed as a candidate 3d KQSL compound. It is predicted and measured to stabilize Kitaev exchange interactions: Co^{2+} has $3d^7$ electronic configurations under octahedral crystal field and $\text{Co}^{2+}\text{-O}^{2-}\text{-Co}^{2+}$ form close to 90° bonds with spin-orbit coupling comparable with other energy scales [19]. Such nearly ideal oxygen octahedron geometry [19] helps suppress Heisenberg and symmetric off-diagonal term [18]. Some calculations predict a ferromagnetic Kitaev interaction [16, 17] while one other [20] and the inelastic neutron scattering measurements [21–24] support dominant antiferromagnetic Kitaev exchange. In both cases, the Kitaev exchange dominates over Heisenberg exchange interactions.

The space group of $\text{Na}_2\text{Co}_2\text{TeO}_6$ is $P6_322$ (No. 182) which is piezoelectric, providing another avenue for tracking phase transitions in high magnetic fields via their effect on electrical properties. The magnetic honeycomb layers of Co^{2+} are separated by nonmagnetic Na^+ layers, which makes $\text{Na}_2\text{Co}_2\text{TeO}_6$ a magnetically quasi-two-dimensional system [19]. In comparison to the Van der Waals systems such as $\alpha\text{-RuCl}_3$, $\text{Na}_2\text{Co}_2\text{TeO}_6$ is struc-

turally more robust and no other stacking sequence of layers has been detected [25].

To explore the ground state and its evolution under magnetic field, several phase diagrams were constructed in the literature [22, 26–28]. However, these studies do not all extend to magnetic saturation and certain phase boundaries still need a closer investigation as they may surround a KQSL phase. Furthermore, although the ground state at low temperature in zero field is well established to be antiferromagnetic [29], its spin structure is still under debate. A zigzag structure [29] similar to $\alpha\text{-RuCl}_3$ [30] was initially adopted due to many common behaviors observed in both systems [22]. The detected magnon dispersion from neutron diffraction can also be well fitted using models based on the zigzag spin structure despite the discrepancies in fitting parameters among different studies [21, 23, 31, 32]. However, more recent inelastic neutron scattering [33] and nuclear magnetic resonance studies [34] proposed a triple-Q order as the ground state spin structure. We also note that due to two slightly different Co environments, a small ferrimagnetic magnetization was observed. [35].

Multiple phase transitions are observed in $\text{Na}_2\text{Co}_2\text{TeO}_6$ with applied magnetic field but only one is established at about 9.5 T as the transition into a mostly spin polarized phase from magnetization and specific heat measurements [26, 35]. For instance, a metamagnetic phase transition is observed in polycrystals at about 6 T, mimicking a transition in $\alpha\text{-RuCl}_3$ in many aspects such as the onset of a plateau in field-dependent magnetic entropy and the appearance of an additional electron spin resonance mode [22]. This transition is more clearly revealed in single crystals as an anomaly in magnetization and thermal conductivity measurements when magnetic field is applied along a^* -axis [22, 26]. This new phase, which resembles the putative KQSL phase in $\alpha\text{-RuCl}_3$ was considered also a spin disordered phase [22]. However, because of the lack of enough data points, the phase boundaries are not well defined and the nature of this phase is still not clear. Additionally, another phase boundary was observed at about 8 T in thermal conductivity measurement with magnetic field applied along both a - and a^* -axis [26] and in torque magnetometry along a^* -axis [28]. This phase, instead of the above mentioned, is recently proposed to be a KQSL phase from torque magnetometry and inelastic neutron scattering study [22], but this also needs further confirmation from other measurements. Thus, it is necessary to establish a more complete phase diagram built from many different experimental techniques that reaches the full saturation of the magnetization to clarify the behavior of this material.

In this work, we construct comprehensive temperature-magnetic field ($\mathbf{T}\text{-}\mathbf{H}$) phase diagrams along both a - and a^* -axes based on the magnetic, thermodynamic, electric, and elastic properties of $\text{Na}_2\text{Co}_2\text{TeO}_6$. We also investigate a partial phase diagram for $\mathbf{H} \parallel \mathbf{c}$. We observed a series of three phase transitions in magnetic fields for

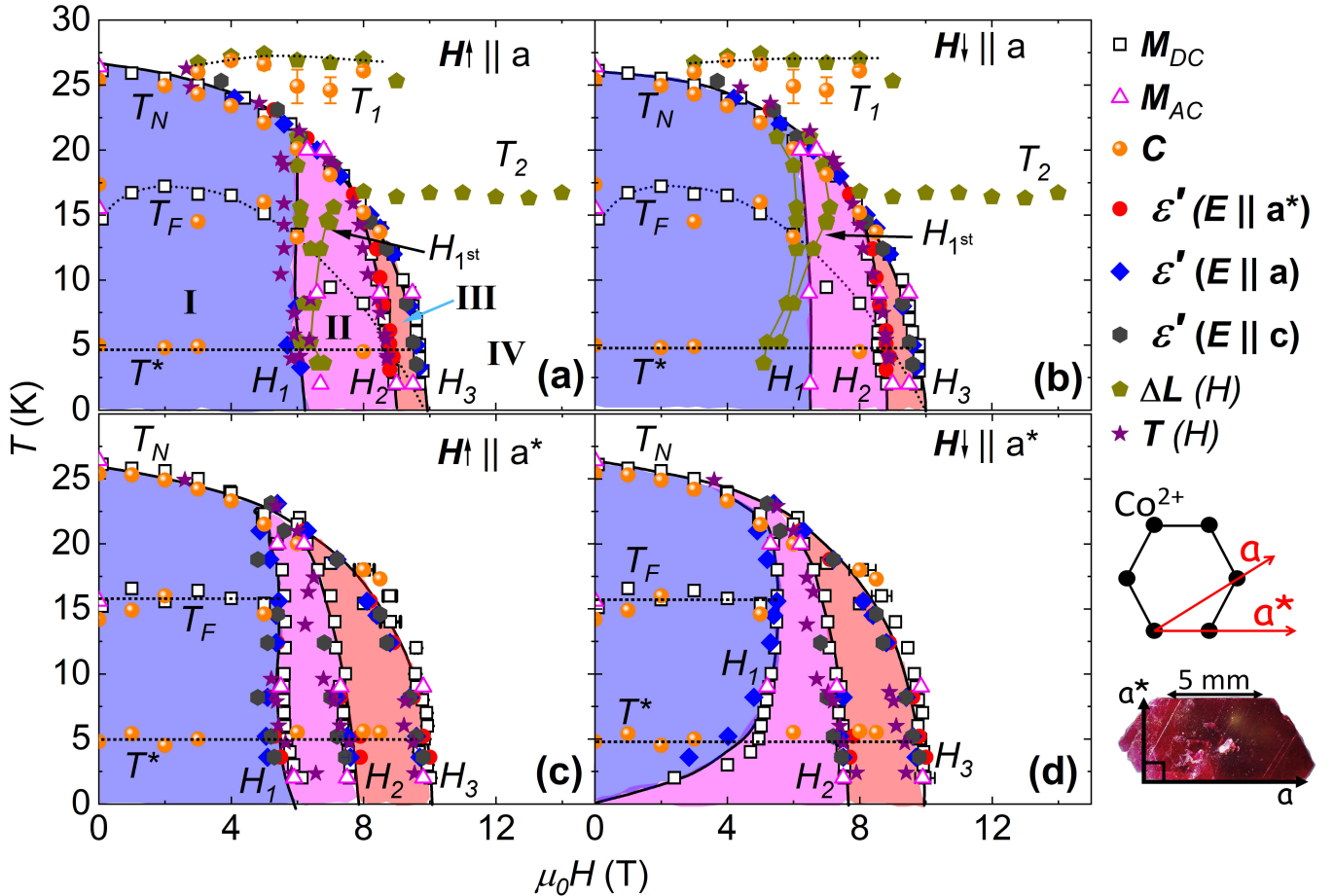


FIG. 1. Phase diagrams for $\mathbf{H} \parallel a$ (panel (a) and (b)) and $\mathbf{H} \parallel a^*$ (panel (c) and (d)) constructed from magnetization M , specific heat C , dielectric constant ϵ' for three directions of the applied electric field \mathbf{E} as indicated, magnetostriction $\Delta L(H)$, and magnetocaloric effect $T(H)$. $H \uparrow$ and $H \downarrow$ are the up and down sweeps of the magnetic field, respectively. The solid or dotted lines are guides to the eyes. The hexagon in the legend defines the a - and a^* -axes with respect to the honeycomb lattice of Co^{2+} . At the bottom right is a photo of a single crystal with a - and a^* -axes indicated.

$\mathbf{H} \parallel a$ and a^* . The critical fields for the a and a^* field axes are significantly different. This is more consistent with the zigzag magnetic ordering at low fields as it naturally has drastically different spin configurations along a - and a^* -directions. In addition, we do not observe temperature or field-dependent electric polarization onsetting at any of the magnetic phase boundaries in both single-crystals along a^* -axis with $\mathbf{H} \parallel a$ -axis and in a large polycrystal. This also favors the zigzag spin structure scenario whose symmetry does not support electric polarization, whereas the triple-Q structure should produce an electric polarization under magnetic field (see supplemental information - S.I.[36].) We do see strong coupling between magnetic and electric order parameters evidenced by magnetic field and temperature-dependent dielectric constants and peaks in the dielectric constant at some field-induced phase transitions, without concomitant peaks in the magnetostriction. At high fields for $\mathbf{H} \parallel a$ and a^* we repeatedly observed additional phase transitions as a function of temperature in

dilatometry and heat capacity. These may indicate subtle structural changes. Finally, when $\mathbf{H} \parallel c$ -axis, the system does not reach saturation even at 60 T as indicated by magnetization measurement (Fig. S4 of the S.I. [36]). Five phase regions are observed all below 16 T as shown in Fig. S5 of the S.I. [36]. The dielectric constant is shown to be independent of magnetic field and the temperature-dependent dielectric constant revealed three broad humps that do not match with any of the magnetic transitions observed in magnetization measurements. This suggest that the Na^+ layer decouples from the magnetic and properties of $\text{Na}_2\text{Co}_2\text{TeO}_6$ and the dielectric humps are most likely due to Na^+ freezing as temperature decreases.

II. EXPERIMENTS

A. Crystal growth

The single crystals were grown by the flux method. A polycrystalline sample of $\text{Na}_2\text{Co}_2\text{TeO}_6$ was mixed with a flux of Na_2O and TeO_2 in a molar ratio of 1:0.5:2 and gradually heated to 900 °C at 3 °C/min in the air after grinding. The sample was kept at 900 °C for 30 hours and then was cooled to a temperature of 500 °C at the rate of 3 °C/hour. The furnace was then shut down to cool to room temperature. Crystal structure and purity was verified by X-ray diffraction and carefully oriented using Laue X-Ray diffractometer. Consistent magnetic susceptibilities of different single crystalline samples used in this work confirm that all samples maintain the same crystal qualities and retain the same magnetic properties.

B. Magnetization, Specific heat, and Dielectric constant

Vibrating sample magnetometry and specific heat measurements were performed in a 14 T Quantum Design Physical Property Measurement System (PPMS) using the built-in options with the magnetic field aligned along both a - and a^* -axes. Specific heat was obtained down to 1.9 K using the standard semi-adiabatic heat pulse method in the PPMS. To align the field orientation, one edge of a single crystal sample (0.54 mg) was carefully adjusted and mounted on the stage of the PPMS vertical puck. The electric capacitance as a function of magnetic field was measured using an Andeen-Hagerling AH2700A capacitance bridge at 12 kHz with a custom-built co-axial cable probe in the PPMS. The electrodes were deposited on opposite faces of $\text{Na}_2\text{Co}_2\text{TeO}_6$ using silver epoxy (EPO-TEK H20E) to form a parallel-plate capacitance geometry. The areas of the electrodes for the a (a^*) direction were 0.28 mm² (1.11 mm²) and the distance between the two electrodes was 0.46 mm (0.49 mm). Pt wires were used to electrically connect the electrodes on the samples to adjacent coaxial cables that in turn lead to the room temperature electronics. Temperature-dependent capacitance was also measured at different frequencies using the same probe and samples but with an LCR Meter (Keysight E4980A). Electrical polarization measurements were performed by the standard technique of integrating the current between ground to the electrical contacts as the temperature or magnetic field changes. These measurements were performed on single- and polycrystals both in pulsed fields using a Stanford Research 570 current to voltage converter [37, 38], and in a PPMS using a custom coaxial cable probe and a Keithley 6517A electrometer. Single crystals used here are the same pieces as used in the dielectric constant measurements as discussed above, and the electrical connections on polycrystals are prepared in the same way as well. The area of the electrode on the

polycrystal was 7.23 mm² and the distance between the two electrodes was 0.71 mm.

C. Magnetocaloric effect

The magnetocaloric effect (sample temperature change vs magnetic field) measurement was performed in pulsed magnetic fields. In this measurement, an adiabatic condition was realized due to the ultra-fast field sweeping rate of \sim 10,000 T/s. To obtain a strong thermal link between the sample and the thermometer on millisecond timescales in pulsed fields, a semiconducting AuGe thin film with a thickness of 10 nm was directly deposited on the surface of the sample as a thermometer by RF magnetron sputtering at 40 mTorr pressure of ultra-high purity Ar gas for 60 minutes with 100 W power [39]. Au contact pads were then deposited on top of the AuGe film with a shadow mask, leaving a stripe of AuGe uncovered. A custom digital lock-in method with 100 kHz source current is used to measure the thermometer resistance in pulsed fields, with four point contacts, as is usually employed at the NHMFL-PFF. A detailed cartoon picture of the thermometer can be found in the S.I. [36]. The thermometers were calibrated in thermalized conditions with exchange gas to obtain resistance vs temperature and an identical reference thermometer was used to obtain the magnetoresistance calibration.

D. Thermal expansion/Magnetostriction

Length changes of the sample were measured as a function of temperature (thermal expansion) and magnetic field (magnetostriction). The Fiber Bragg Grating (FBG) dilatometry measurement was used in the PPMS using a custom-built probe and optical fibers with 2 mm Bragg gratings [40]. A straight edge of the as-grown plate-like single crystal of $\text{Na}_2\text{Co}_2\text{TeO}_6$ was carefully attached to the optical fiber using Henkel Ultragel superglue. A Pt wire connected the sample to the Cernox temperature sensor, providing a proper thermal link between the two and to the bath. The FBG spectra were recorded using an optical sensing interrogator (Micron Optics, si155). The a - and a^* -axis data were recorded *in situ* with a third Bragg Grating as a reference to be subtracted from the sample signals [40]. The obtained thermal expansion as a function of magnetic field and temperature are normalized respectively following $\Delta L(H, T_0) = \Delta L(H, T_0)/\Delta L(0, T_0)$; $\Delta L(H_0, T) = \Delta L(H_0, T)/\Delta L(H_0, 3.3\text{K})$. An illustration of the configuration of the sample attachment can be found in Ref. [36]. To ensure reproducibility, two different pieces of samples were measured for each crystallographic orientation. To eliminate the effect from the superglue, for each orientation one sample was measured twice with re-gluing in between.

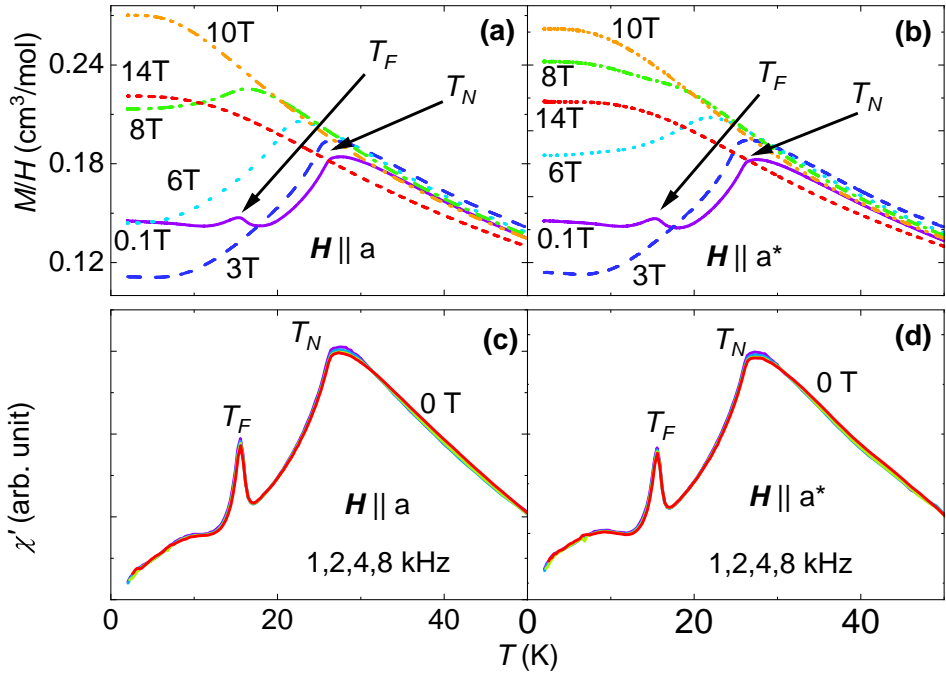


FIG. 2. Longitudinal DC magnetic susceptibility M/H vs T for various magnetic fields between 0.1 and 14 T along a (a) and a^* (b). AC magnetic susceptibility χ' vs T for fields along the a axis (c) and a^* axis (d). The AC field with amplitude 10 Oe is applied at 1,2,4, and 8 kHz with a DC field $H = 0$. T_F and T_N are the temperatures recorded in the phase diagram. The complete data sets are available in the S.I. [36].

III. RESULTS

From the above-mentioned measurements, we constructed comprehensive T - H phase diagrams of $\text{Na}_2\text{Co}_2\text{TeO}_6$ as illustrated in Fig. 1 with field along both a - and a^* -axis. A phase diagram with $\mathbf{H} \parallel c$ constructed from magnetization measurements can be found in the S.I. [36]. For clarity, we discuss an overview of the phase diagram before describing the details of the individual measurements below. From field-dependent measurements, there are four successive phases (I-IV) including the polarized phase, separated by the critical fields H_1 , H_2 , and H_3 . The first two phase boundaries are largely independent of temperatures whereas H_3 is mean-field-like. On the other hand, from temperature-dependent measurements, three major phase boundaries are observed as T_N , T_F , and T^* , consistent with the literature [26, 27, 35]. We tracked T_F to higher fields than previously reported. It is noteworthy that the T_F boundary is qualitatively different when magnetic field is applied along a - or a^* -axes. It is field-dependent and persists into region II when magnetic field is applied along a -axis whereas it becomes field independent and stops within region I when magnetic field is applied along a^* -axis. Several additional critical fields/temperatures (T_1 , T_2 and $H_{1^{st}}$) were also observed in thermal expansion and heat capacity measurements.

Fig. 2 (a) and (b) show the DC magnetic susceptibility

(M/H) as a function of T taken at various magnetic fields H between 0.1 T and 14 T applied along a and a^* , respectively. T_N indicates the antiferromagnetic phase transition temperature ≈ 27 K for both directions, consistent with other results [22, 25, 29, 34, 35, 41]. Another peak at around 16 K and 0.1 T, denoted with T_F , is also observed for both directions. This feature has been interpreted as a signature of spin canting [22] and it is the temperature at which a low-energy broad excitation spectra turn into a clear magnon band [33]. The peak at T_F is quickly suppressed as the applied magnetic field increases from 0.1 T to 1 T so that its feature is only clearly visible in the derivatives at higher fields (see S.I. [36]). On the other hand, T_N shifts towards lower temperatures and the feature becomes broadened with increasing field as and eventually disappears above 8 T. The DC susceptibility at 2 K decreases monotonically above 10 T as the system enters the partially spin polarized phase.

Fig. 2 (c) and (d) display the AC magnetic susceptibility (χ') respectively along a - and a^* -axes as a function of T taken under four different frequencies. No frequency dependence is observed below 8 kHz up to 100 K, in contrast with the frequency-dependent dielectric constant (see Fig. S7 of the S.I. [36]). This observation suggests that the features observed in the temperature-dependent dielectric constant originate from Na^+ configurations and are not related to any magnetic properties.

Fig. 3 (a)-(c) and (f)-(h) illustrate the DC magnetization ($M(H)$) at various T when H is applied along a -axis. Magnetization and its first and second derivatives

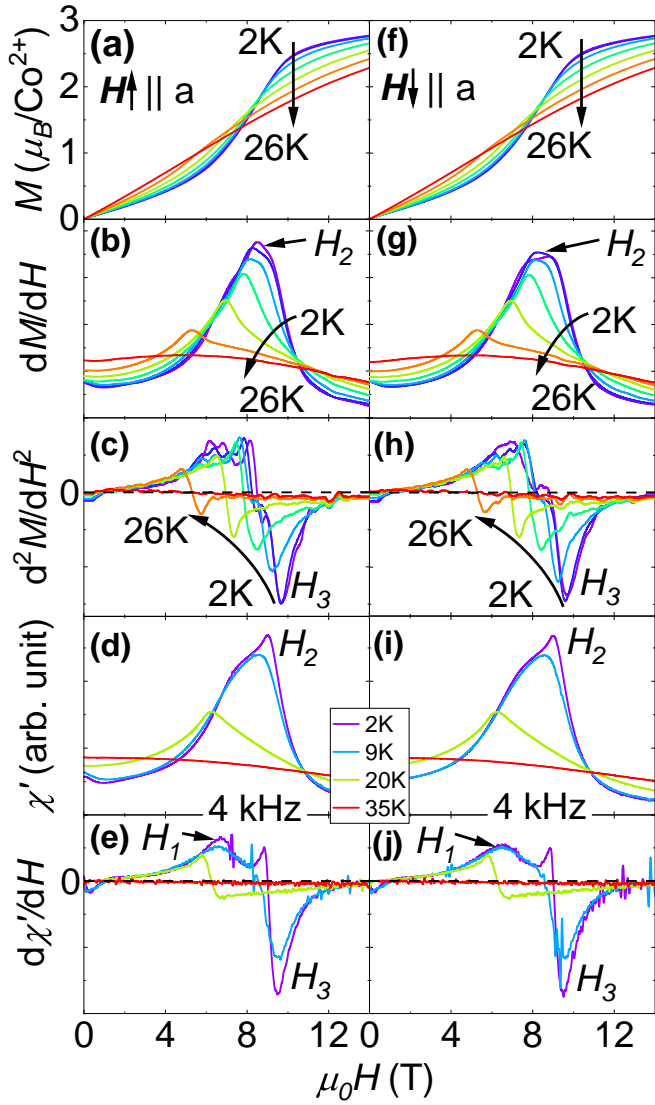


FIG. 3. DC Magnetization M and AC magnetic susceptibility χ' and their first, and second derivatives with respect to magnetic field H as a function of $\mathbf{H} \parallel \mathbf{a}$ taken in superconducting magnets. (a)-(e) display the up field-sweep ($H \uparrow$) data in which (a)-(c) and (d)-(e) are from DC and AC measurements, respectively. (f)-(j) display the down field-sweep ($H \downarrow$) data in which (f)-(h) and (i)-(j) are from DC and AC measurements, respectively. All AC magnetic susceptibility data shown here are measured at 4kHz. $H_{1,2,3}$ are the critical fields recorded in the phase diagram. The complete data sets are available in the S.I. [36].

of up (down) field-sweeps are presented in Fig. 3 (a), (b), and (c) ((f), (g), and (h)), respectively. Data curves from up and down field-sweeps overlap with each other showing no hysteresis, consistent with previous reports [22, 34, 35]. Here we define H_2 as the inflection point of the magnetization curves found from the peak in the first derivative magnetization (Fig. 3 (b) and (e)) and H_3 is the maximum curvature point defined as the peak in the second derivative in Fig. 3 (c),(f). While the H_3 phase

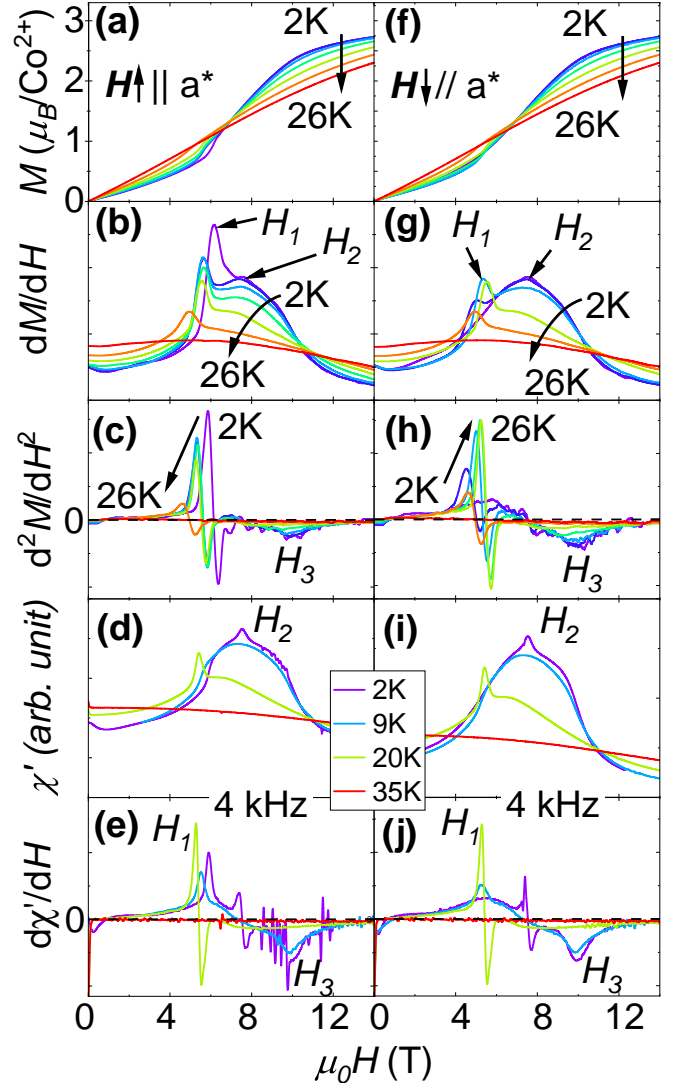


FIG. 4. DC Magnetization M and AC magnetic susceptibility χ' and their first, and second derivatives with respect to magnetic field H as a function of $\mathbf{H} \parallel \mathbf{a}$ taken in superconducting magnets. (a)-(e) display the up field-sweep ($H \uparrow$) data in which (a)-(c) and (d)-(e) are from DC and AC measurements, respectively. (f)-(j) display the down field-sweep ($H \downarrow$) data in which (f)-(h) and (i)-(j) are from DC and AC measurements, respectively. All AC magnetic susceptibility data shown here are measured under 4000 Hz. $H_{1,2,3}$ are the critical fields recorded in the phase diagram. The complete data sets are available in the S.I. [36].

boundary is consistent with those found in previous thermal conductivity and magnetization works [26, 35], H_2 has not been called out in all previous works, despite subtle features consistently observed in previous reports [22, 26, 35]. Above H_3 , the magnetization increases with a downward curvature consistent with saturation. However a small linear component in $M(H)$ persists up to the highest measured fields of 60 T (Figure 5), likely due to Van Vleck paramagnetism [42]. The strong spin-orbit

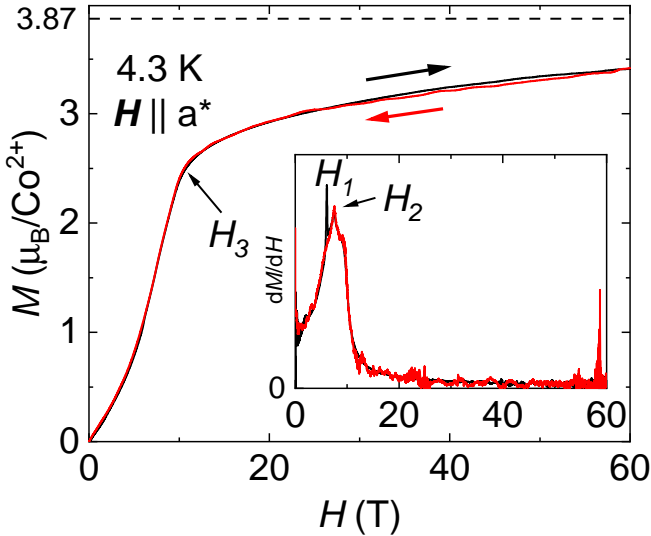


FIG. 5. Magnetization M as a function of magnetic field H applied along a^* -axis measured in millisecond pulsed fields to 60 T at 4.3 K. The black and red lines are up- and down-sweeps, respectively. The inset is the derivative dM/dH .

coupling enhances the g-factor anisotropy which leads to the large saturation magnetization value near $3 \mu_B$, obtained by removing the linear Van Vleck contribution.

AC magnetic susceptibility (χ') and its first derivative along a -axis are shown in Fig. 3 (d)-(e) and (i)-(j) for the up and down field-sweeps, respectively. All of H_1 through H_3 are observed with similar temperature evolution compared to DC measurements. H_1 and H_3 are defined as peak and dip in the first derivative and H_2 is defined as the peak in χ' . Note that H_1 is only observed in AC measurement, likely because it is too subtle to observe in DC measurements.

Results of DC magnetization ($M(H)$) and its first and second derivatives at various T when H is applied along a^* -axis are shown in Fig. 4 (a)-(c) and (f)-(h) for field up- and down-sweeps, respectively. Three phase boundaries, H_1 through H_3 , are observed in this direction. H_1 and H_2 are defined as the peak positions in the first derivative and H_3 is defined as the peak position in the second derivative of magnetization. In contrast to the a -axis data, there is noticeable hysteresis beginning at H_1 below 26 K ($\approx T_N$), as shown more clearly in Fig. S3 in the S.I.[36], consistent with previous reports [22, 34, 35]. With increasing temperature, all critical fields shift towards lower fields with peak height decreasing for both up and down field-sweeps except for the H_1 peak in down-sweeps whose amplitude increases with increasing temperature. Similar to the magnetization with $H \parallel a$, we observed the linearly increasing magnetization above the saturation magnetization because of the Van Vleck paramagnetism and large g-factor anisotropy from the strong spin-orbit coupling.

Fig. 4 (d)-(e) and (i)-(j) illustrates the AC susceptibility (χ') and its first derivative along a^* -axis for the up

and down field-sweeps, respectively. All of H_1 through H_3 are observed with similar temperature evolution compared to DC measurements. H_1 and H_3 are defined as peak and dip in the first derivative and H_2 is defined as the peak in χ' . In the 9 K up-sweep data, below 3 T and above 12 T, data show significant extrinsic noise but it occurs away from phase boundaries.

In order to check if there are no additional magnetic phase transitions, we measured the magnetization with $\mathbf{H} \parallel a^*$ up to 60 T using pulsed-field magnet at 4.3 K as shown Fig. 5. The low-field section of the data agrees with DC measurements, as illustrated more clearly by dM/dH in the inset. We did not observe any additional magnetic phase transition above H_3 , confirming that magnetization saturates above H_3 .

Next, we investigate the electrical properties of $\text{Na}_2\text{Co}_2\text{TeO}_6$ by measuring the dielectric constant as functions of magnetic field ($\epsilon'(H)$) for various electric and magnetic field directions as shown in Fig. 6. The dielectric constant measurement has been used to determine the phase boundaries of $\alpha\text{-RuCl}_3$ that match well with phase boundaries obtained with other techniques [43, 44]. When the magnetic field is applied along a^* -axis with electric field applied along a^* , a as shown in Fig. 6 (a) and (b) respectively, a similar hysteresis behavior as in the magnetization measurement shown in Fig. 4 is observed. Three phase boundaries H_1 , H_2 and H_3 are clearly visible as peaks in the dielectric constant, and their positions match well with those found in the magnetization. When the electric field is applied along c -axis with $H \parallel a^*$ (Fig. 6 (c)), the peaks corresponding to H_1 , H_2 and H_3 are smaller, though still sharp.

Fig. 6 (d)-(f) shows $\epsilon'(H)$ for $\mathbf{H} \parallel \mathbf{a}$. An additional hump (H_E) is observed when electric field E is applied along a^* -axis. The origin of this feature needs further investigation as it does not overlap with any observations in other measurements. In contrast to the magnetization measurement, hysteretic behavior was observed for $\epsilon'(H)$ for $\mathbf{H} \parallel \mathbf{E} \parallel \mathbf{a}$ as shown in panel (e). The fact that the dielectric constant strongly depends on the magnetic field and magnetic phase transitions are reflected in the dielectric constant suggests that $\text{Na}_2\text{Co}_2\text{TeO}_6$ possesses a fairly strong magnetoelectric coupling. We later discuss the underlying mechanism based on the possible spin structures. For magnetic fields applied along c -axis we observed negligible field dependence in the dielectric constant as shown in the S.I. [36].

The temperature-dependent dielectric constant and dissipation measured at various frequencies are also collected as shown in Fig. S7 of the S.I. [36]. The three pronounced peaks are observed in the dissipative part of the dielectric constant, whose temperatures are dependent on frequency. These do not match any feature seen in the magnetization. We note that Na atoms placed between magnetic layers are disordered at high temperatures and freezes at low temperatures. Therefore, the observed frequency-dependent dissipation could result from Na^+ position freezing.

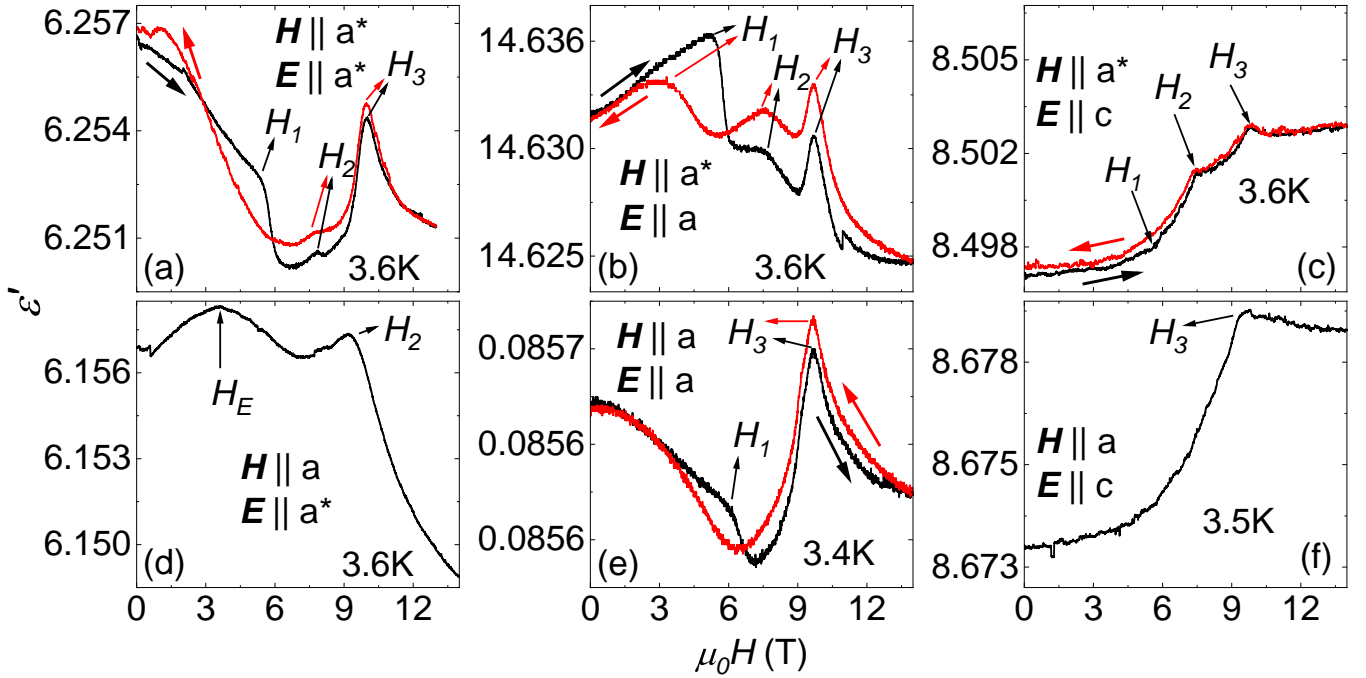


FIG. 6. Dielectric constant $\varepsilon' = \frac{\varepsilon}{\varepsilon_0}$ along all crystallographic orientations as a function of $\mathbf{H} \parallel a$ ((a)-(c)) and a^* ((d)-(f)), taken in a superconducting magnet. Here ε is the dielectric constant of the sample and ε_0 the vacuum. $H \uparrow$ and $H \downarrow$ are the up and down scan, respectively. $H_{1,2,3}$ are the fields recorded in the phase diagram in Fig.1. H_1 in panel (c) is the kink at which the slope of the curve suddenly increases. The complete data sets are available in the S.I. [36].

The thermodynamic properties of $\text{Na}_2\text{Co}_2\text{TeO}_6$ were also investigated and the specific heat divided by temperature (C/T) data are shown in Fig. 7 at various H up to 8.5 T. There is no significant difference between $\mathbf{H} \parallel a$ - and a^* -axes. For both directions, three phase transitions are observed, consistent with our magnetization measurement and previous reports [22, 35]. The T_N peak and T^* hump are observed up to 8.5 T whereas the T_F hump is difficult to extract above 6 T. With increasing magnetic field, the peak at T_N gets weakened and suppressed to lower temperatures whereas the T^* feature is robust against magnetic field. The T_F feature when $\mathbf{H} \parallel a$ is hard to identify at several magnetic field strength but the rest of them show a slight decreasing trend of T_F with increasing magnetic field. When $\mathbf{H} \parallel a^*$, T_F is largely independent of applied magnetic field.

Fig. 8 shows the magnetocaloric effect in quasi-adiabatic conditions in a 65 T pulsed magnet, pulsed to a maximum field of 20 T. The sample temperature as a function of magnetic field is shown on the left axis and its derivative (dT/dH) on the right axis. The magnetic field pulse vs time is shown in the S.I. [36]. The 20 T peak field is chosen so the fast part of the pulse occurs in the region of interest up to 12 T, and the less adiabatic behavior that emerges as the pulse slows down and the field turns around occurs at fields above the region of interest.

We observe hysteresis in $T(H)$ due to the hysteresis originating from the 1st order phase transition at H_1 that

was also seen in the other properties, as well as some thermal relaxation occurring at the highest fields where the field sweep rate slows down and passes through zero, and the adiabatic behavior becomes quasi-adiabatic. We note that with increasing field sweep speed, the hysteresis of 1st order phase transitions generally broadens due to the finite time needed to nucleate and grow the new phase. Thus the hysteresis in H_1 can be expected to open up significantly in these pulsed measurements. In some cases, 1st order phase transitions can be avoided altogether at fast sweep rates due to lack of time for the new phase to nucleate and grow (“supercooling”/“superfielding”). On the other hand, the non-hysteretic 2nd order-like phase transitions at H_2 and H_3 can be observed at similar fields as in DC measurements.

In the $T(H)$ data in Fig. 8 we indicate the phase transitions H_1 , H_2 and H_3 with arrows. These phase transitions appear as minima. This is consistent with increased disorder at a phase transition, which forces the thermal entropy to drop to compensate. H_3 is difficult to observe due to a large background increase in temperature approaching saturation, but can be resolved as a wiggle in dT/dH . These observations are similar to those made for magnetocaloric effect data in $\alpha\text{-RuCl}_3$ [39, 45]. Above H_3 , the temperature increases rapidly. This temperature increase reflects the spin gap that opens above magnetic saturation [26]. E.g. the increase in thermal entropy compensates for the drop in spin entropy as the magnetization saturates and a spin gap opens and increases

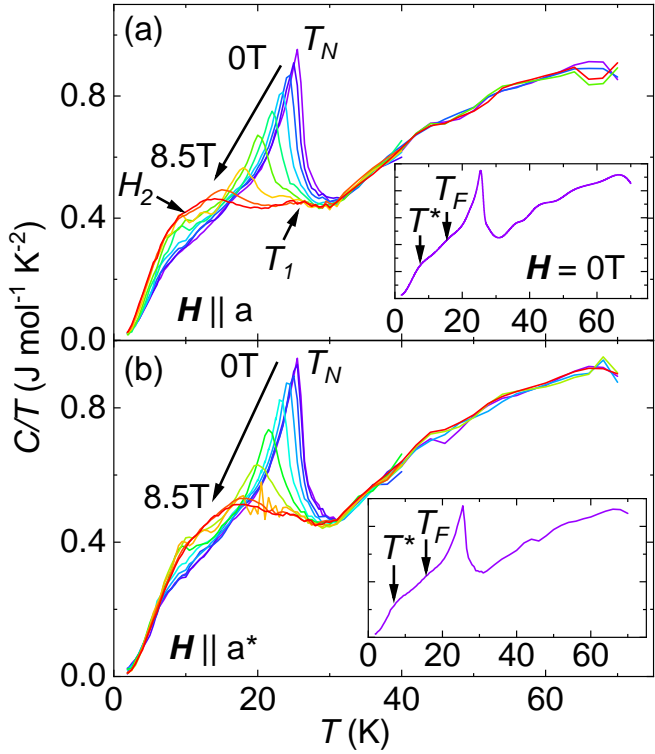


FIG. 7. Specific heat divided by temperature (C/T) as a function of T at various H up to 8.5 T for (a) $\mathbf{H} \parallel a$ and (b) $\mathbf{H} \parallel a^*$. The phase transition temperatures are labeled and corresponding features are indicated by the black arrows. The inset depicts the specific heat data at 0 T for a clearer view of T_F and T^* .

with increasing magnetic field.

When the magnetic field is parallel with a^* , all three phase boundaries are clearly resolved in $T(H)$ as well as dT/dH on the up-sweep. We miss seeing H_1 in the down field-sweep as described above. All of H_1 , H_2 , and H_3 are observed as dips and kinks in the $T(H)$ curve or its first derivative,

We now move to thermal expansion and magnetostriction, e.g. length changes of the sample with temperature and field. Shown in Fig. 9 are the thermal expansion data of $\text{Na}_2\text{Co}_2\text{TeO}_6$ as a function of T with $\mathbf{H} \parallel a$ and a^* up to 14 T. Unlike $\alpha\text{-RuCl}_3$ [39], along both a - and a^* -axes, the thermal expansion ($\Delta a(a^*)/a_0(a_0^*)$) shows very little temperature dependence at zero magnetic field, consistent with previous studies showing no structural transition [25, 29, 46]. However, with increasing field, along the a -axis, a kink at T_1 develops, indicating an onset of slope change. This becomes more and more pronounced with increasing field until 6 T, above which the shape of the thermal expansion *abruptly* changes and a sharp drop appears at T_2 . At even higher fields, the T_2 feature broadens and eventually becomes a gradual decrease. Both features are observed almost always outside the antiferromagnetic phase of $\text{Na}_2\text{Co}_2\text{TeO}_6$ and are independent of magnetic field strength, as illustrated in Fig. 1. On

the other hand, along a^* -axis, all features are broad and we do not identify phase transitions.

The magnetostriction data are shown in Fig. 10. When $\mathbf{H} \parallel a$, a peak is observed in the magnetostriction at 6 - 7 T, corresponding to H_1 , followed by a discontinuous and hysteretic jump at H_{1st} . In the up-sweeps, the amplitude of this jump decreases with increasing temperature until T_F , above which it disappears. But in the down-sweeps, the amplitude of this drop feature increases with increasing T until T_F at which the up- and down-sweep curves overlap with each other. It then suddenly becomes much weaker at higher temperatures and eventually becomes invisible above 22 K. On the other hand, along a^* -axis, only a broad maximum is observed which do not correspond to any phase transitions.

IV. DISCUSSION

Magnetic field versus temperature phase diagrams were built by combining the data from Results. In Fig. 1 we show the phase diagrams for the magnetic field in the plane. The four phase diagram correspond to up and down field sweeps for $\mathbf{H} \parallel a$ and a^* . (In the S.I. [36] we also show the phase diagram for $\mathbf{H} \parallel c$.)

The phase diagrams in Fig. 1 show three phases as a function of magnetic field. These phases are denoted as I, II, and III, and occur in addition to the paramagnetic phase. These three phases contrast with some of the previous studies where only two phases were observed [22, 27], probably due to the limited number of measured quantities or field range in those studies. Recently a study of torque magnetometry and inelastic neutron scattering also showed some evidence of all three phases [28].

For $\mathbf{H} \parallel a$ we also observe apparent phase transitions T_1 and T_2 as a function of temperature in the thermal expansion and heat capacity at high fields that were not previous reported. Our comprehensive phase diagrams reveal a couple of interesting features of those phases. First, the phase boundaries H_1 and H_2 are nearly independent of temperature. Successive temperature-independent phase boundaries are not often observed except for in frustrated magnets [39, 42, 47–50]. Therefore, this observation supports the existence of magnetic frustration in $\text{Na}_2\text{Co}_2\text{TeO}_6$, which is expected from Kitaev interactions as well as off-diagonal symmetric anisotropy, Γ terms [51, 52]. Among these phase transitions, the H_1 boundary along the a^* -axis is clearly 1st order, showing hysteresis between up and down field sweeps and metamagnetic behavior with a sudden change in magnetization (Fig. 4). Considering that the spins are aligned along the a -axis in $\text{Na}_2\text{Co}_2\text{TeO}_6$ [25], this is different from a simple spin-flop or spin-flip phase transitions.

We find that H_1 involves a rather large and discontinuous lattice distortion.

Recent inelastic neutron scattering and thermal conductivity measurements [26, 28] suggest that the phase

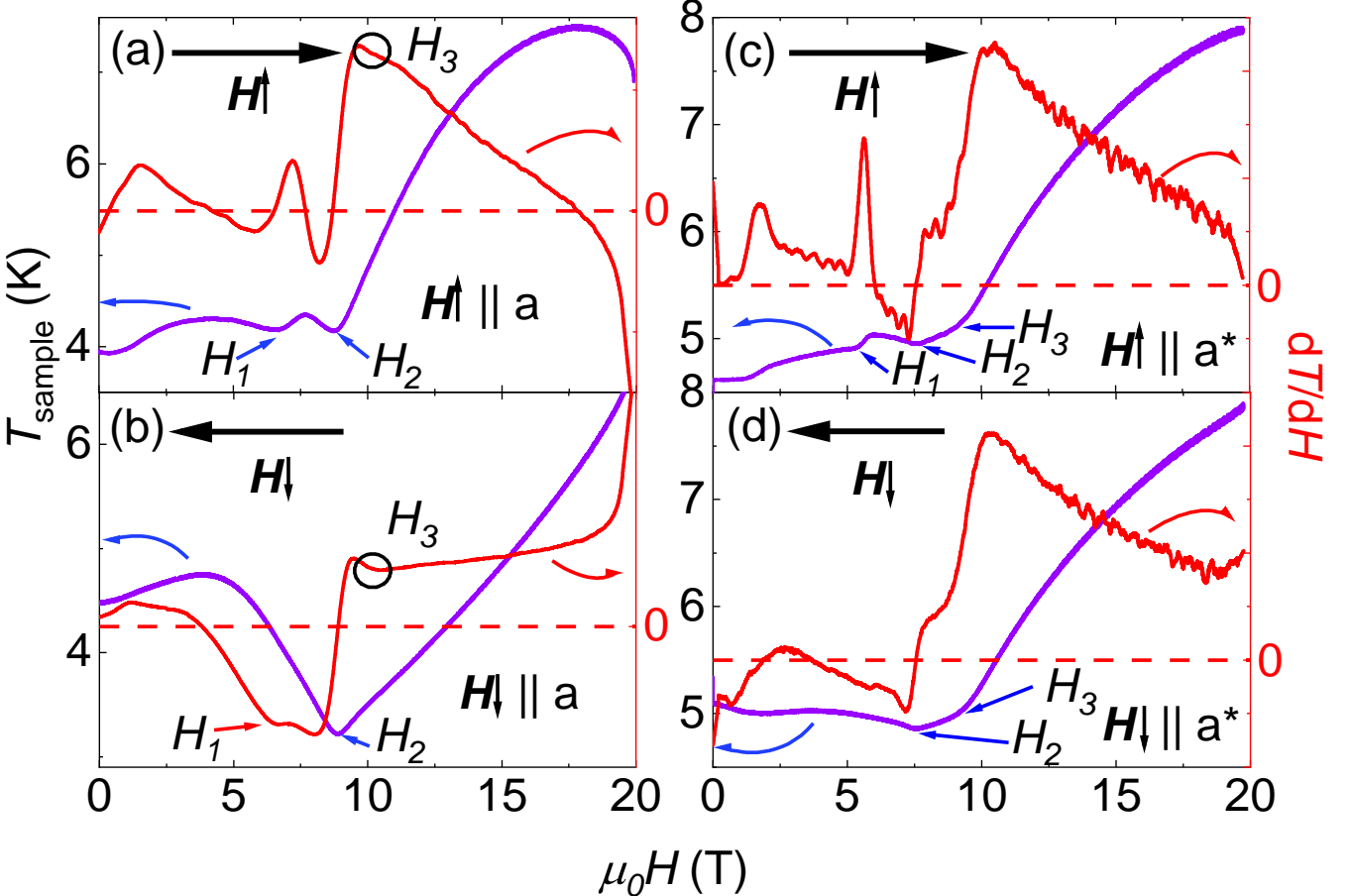


FIG. 8. Magnetocaloric effect measurements in millisecond pulsed magnetic fields. Sample temperature T_{sample} as a function of H applied along both a -axis ((a),(b)) and a^* -axis ((c),(d)). The blue lines are the sample temperatures and the red lines are the derivatives ($\frac{dT}{dH}$). Phase boundaries revealed in Fig. 1 are labeled and indicated by arrows and circles. The dashed red lines are indications of $\frac{dT}{dH} = 0$. The field sweep directions are further illustrated at the top of each plot.

between H_2 and H_3 could possibly be a Kitaev quantum spin liquid. It shows a return to six-fold symmetry in the hexagonal plane, and a broad region of low-lying excitations. Further studies are needed to distinguish KQSL from disordered or other possible phases.

We begin the discussion with the properties of phase I. The zero-field magnetic long-range ordering occurs around 27 K (T_N) and two subsequent phase transitions around 15 K (T_F) and 5 K (T^*) are observed, consistent with other literature and therein their natures are discussed [22, 27]. One major debate for $\text{Na}_2\text{Co}_2\text{TeO}_6$ is the zigzag versus triple-Q spin structure for this state [25, 33]. We argue that the zigzag spin structure is more likely in Region I for the following reasons. Combined with the crystal symmetry, the zigzag spin structure has a magnetic point group of 2221' (No. 6.2.18) regardless of whether the ground state is purely antiferromagnetic or ferrimagnetic as reported in [35]. This point group forbids spontaneous electric polarization or magnetic field-induced electric polarization as it has twofold rotational symmetry along all three directions. On the other hand,

although the triple-Q spin structure also does not allow the spontaneous electric polarization, it is expected to possess a linear magnetoelectric coupling having a magnetoelectric tensor with non-zero off-diagonal components within the plane (see S.I. [36]). Thus electric polarization should emerge in magnetic fields and flip sign as the magnetic field sign is flipped. To distinguish between these two cases we performed electric polarization measurements with and without electric poling, e.g. electric fields applied on cooling across the phase transitions and also electric fields applied while sweeping the field. We observed no noticeable feature in the measurement (see S.I. [36]) despite the pronounced features observed in dielectric constant as a function of magnetic field and magnetostriction measurements. Therefore, our results strongly suggest the zig-zag spin structure for region I. Furthermore, anisotropic magnetic field dependent T_F , and strongly anisotropic field dependent magnetization, also appears more consistent with a zigzag, not triple-Q, structure [21, 25, 53].

When magnetic field is applied along a -axis in phase

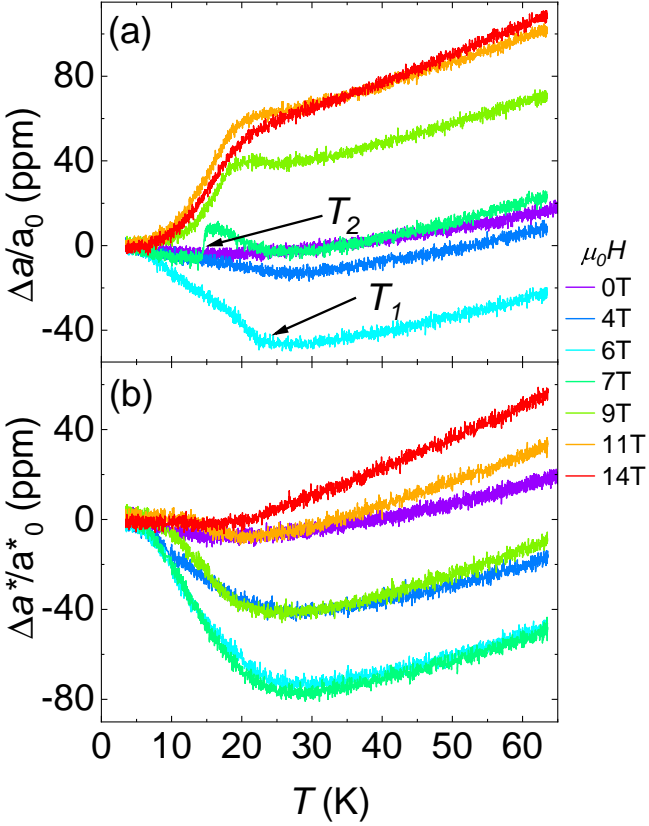


FIG. 9. Thermal expansion $\Delta a/a_0$ as a function of temperature T in (a) a - and (b) a^* -axes with various magnetic fields H applied along the same direction as the length change. $T_{1,2}$ represent the phase boundaries/crossovers recorded in the phase diagram. All data curves are normalized to the corresponding lowest-temperature thermal expansion values. The complete data sets are available in the S.I. [36].

I, the 1st order H_1 phase transition to another anti-ferromagnetic phase (Region II) is clearly revealed in AC magnetic susceptibility (Fig. 3), dielectric constant (Fig. 6), magnetocaloric effect (Fig. 8), and magnetostriction (Fig. 10) in up sweeps. The transition involves a strong lattice contraction along a -axis. Similar behaviors in magnetostriction and magnetocaloric effect have been observed in α -RuCl₃ [39, 54], which were interpreted as a signature of a phase transition from the zigzag spin structure to a noncoplanar spin structure characterized by a larger magnetic unit cell consisting of three inequivalent pairs of parallel spins [55].

Moving on to $\mathbf{H} \parallel \mathbf{a}^*$ for H_1 , the phase boundary is observed in DC magnetization and AC magnetic susceptibility both with a small hysteresis loop (Fig. 4, refSUPP-Magnetization-inPlane of the S.I. [36]), dielectric constant (Fig. 6), and magnetocaloric effect measurements (Fig. 8). One obvious difference compared to $\mathbf{H} \parallel \mathbf{a}$ is that for $\mathbf{H} \parallel \mathbf{a}^*$, the H_1 feature is more pronounced in DC magnetization measurements. This is not unreasonable as antiferromagnetic transitions are not always revealed in magnetization measurements. Another notice-

able difference between a - and a^* -axes is the dielectric constant. H_1 is observed regardless of electric field directions when $\mathbf{H} \parallel \mathbf{a}^*$ but only with $E \parallel a$ when $\mathbf{H} \parallel a$. Additionally, the H_0 phase boundary observed in magnetostriction may also be a shifted version of the H_1 boundary, as mentioned previously. We note that region II has different lattice constants from the zig-zag anti-ferromagnetic ground state due to the 1st order phase transition at H_1 . An open question is whether there is a space group change at H_1 . Further investigation such as neutron diffraction and X-ray measurements in magnetic field are necessary to investigate this.

The H_2 phase boundary is similar for $\mathbf{H} \parallel \mathbf{a}$ and \mathbf{a}^* directions. It is observed in DC magnetization, AC susceptibility (Fig. 3, 4), dielectric constant (Fig. 6), and magnetocaloric effect (Fig. 8) measurements. It manifests as a dip ($\mathbf{H} \parallel a$) or a kink ($\mathbf{H} \parallel a^*$) in $T(H)$ curves where the sample temperature starts to increase monotonically with increasing field. Such increase in lattice entropy in turn indicates a decrease in spin entropy in region III under an quasi-adiabatic condition. Phase III is the putative KQSL phase according to the resumption of the hexagonal symmetry in magnetic torque measurements, inelastic neutron diffraction measurements [28], and low-lying magnetic excitations in thermal conductivity [26]. It is counter-intuitive that the entropy would decrease going from an ordered to a spin liquid phase, as we observe. However, we note that for KQSL-candidate α -RuCl₃ the same entropy decrease was observed [39].

As reported in the literature [26, 35], the H_3 phase boundary appears like a continuation of the T_N boundary from magnetization and specific heat measurements, with a mean-field-like shape in field-temperature. However, this phase boundary encompasses multiple magnetic phases I, II and III. Note that when $\mathbf{H} \parallel a$, H_3 is only clearly observed in DC magnetization, AC magnetic susceptibility and dielectric constant measurements, but for $\mathbf{H} \parallel a^*$, its feature is also very pronounced in the magnetocaloric effect.

Above H_3 , the DC magnetization vs magnetic field becomes convex, appearing to saturate, as explained in the previous section. The temperature of the sample from the magnetocaloric effect continuously increases, consistent with a spin gap opening with increasing magnetic field. These two features support that Region IV is the spin polarized phase albeit with a magnetization that continues to slightly increase linearly up to at least 60 T due to a Van Vleck effect. A peak in the dielectric constant is usually associated with a phase transition involving electric dipole moments. As our electric polarization measurement did not yield any net electric polarization in this compound, such an electric ordering would have to be an antiferroelectric or disordered arrangement. The idea that Majorana excitations out of the KQSL phase create electrical patterns has been proposed for α -RuCl₃, though there the electric patterns have no net dipole as they are radially symmetric [56]. In general, magnetic spin configurations are known to produce electric polar-

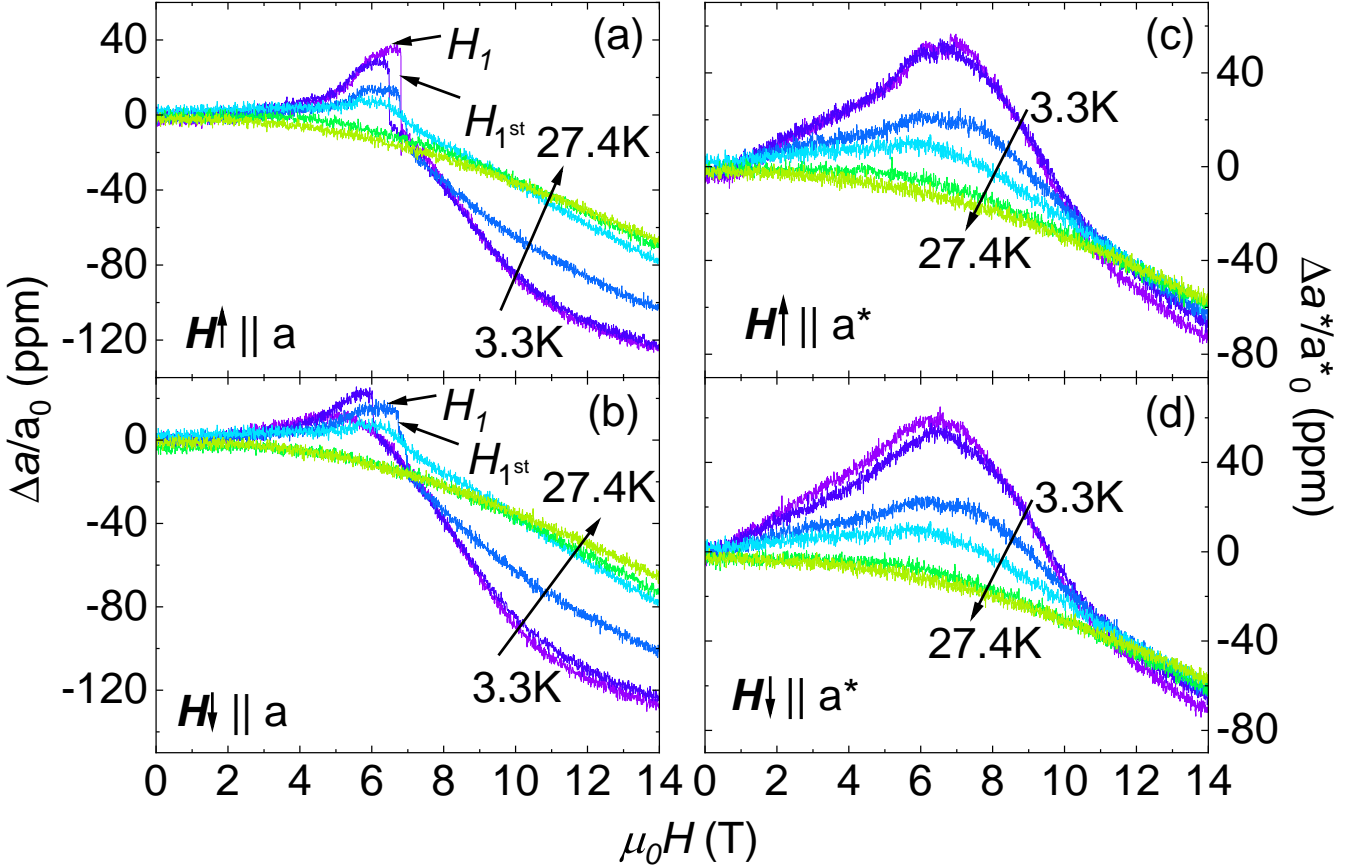


FIG. 10. Magnetostriction as a function of applied magnetic field H in a superconducting magnet taken at various temperatures as indicated for both a -axis ((a), (b)) and a^* -axis ((c), (d)). $H \uparrow$ and $H \downarrow$ are the up and down field sweeps, respectively. H_0 and H_{1st} are the phase boundaries/crossovers recorded in the phase diagram. All data curves are normalized to the corresponding zero field thermal expansion values. The complete data sets are available in the Ref. [36].

ization when the magnetism in conjunction with the lattice creates a polar axis, or alternatively magnetic configurations can create local dipoles that cancel each other in the bulk preventing a net electric polarization. Here, the possibility that a putative KQSL phase or its excitations such as Majorana anyons could carry electric dipoles in $\text{Na}_2\text{Co}_2\text{TeO}_6$ needs to be investigated.

Finally we note that for $\mathbf{H} \parallel \mathbf{a}^*$ there is an apparent tricritical point where T_N , H_2 and H_3 meet. If these are all 2nd order phase transitions, such a tricritical point is not allowed by symmetry [57] or free energy continuity arguments [58]. One possibility is one of these phase boundaries is not a 2nd order phase transition. Another possibility is that this tricritical point merges with the first-order H_1 phase boundary, though this isn't fully supported by our data. For $\mathbf{H} \parallel \mathbf{a}$, there is no observed tricritical point of 2nd order phase transitions due to the addition of the T_2 phase line. We note also that where T_1 joins T_N there may be a tricritical point, but more likely T_1 joins T_N at $H = 0$, removing that conundrum.

V. CONCLUSION

In this work we established a comprehensive T - H phase diagram of $\text{Na}_2\text{Co}_2\text{TeO}_6$ based on its magnetic, electric, thermodynamic, and elastic properties. Three successive field-induced magnetic phases (I, II, III) are observed before magnetic saturation whose phase boundaries (H_1 , H_2) are largely independent of temperature. This suggests the existence of magnetic frustration and thus, Kitaev and off-diagonal interactions in the system. Moreover, the dielectric constant is heavily dependent on magnetic field and it reveals all of the magnetic phase transitions, indicating a strong magnetoelectric coupling in $\text{Na}_2\text{Co}_2\text{TeO}_6$ though without a measurable net electric polarization. Of the two proposed magnetic ground states in region I at zero magnetic field, the zigzag state fits our data better. By symmetry the zigzag state should not show an electric polarization in zero or applied fields, consistent with our measurements. Another argument in favor of the zigzag phase is the drastic differences between the physical properties for magnetic field along the a - and a^* -axes, which is qualitatively more consistent with the zigzag phase. The microscopic nature of Region II and III

are still under investigation. But our work indicates that Region II has a different lattice constants compared to those in Region I, and Region III has lower entropy than Region II, in which the spins start to line up with the applied magnetic field. At even higher fields, $\text{Na}_2\text{Co}_2\text{TeO}_6$ enters the spin polarized phase where a spin gap opens. Strong peaks in the dielectric constant at the boundary between Region III and magnetic saturation are consistent with an antiferroelectric or disordered-electric phase transition in conjunction with the magnetic one.

VI. ACKNOWLEDGEMENT

This work was supported by the U.S. Department of Energy, Office of Science, National Quantum Information

Sciences Research Centers, Quantum Science Center. The facilities of the National High Magnetic Field Laboratory are supported by the collaborative grant DMR-1644779 by the National Science Foundation, the State of Florida and the Dept of Energy. Q. H. and H. D. Z. grew the samples with support from the National Science Foundation grant DMR-2003117. M. L. also acknowledges LDRD program at Los Alamos National Laboratory.

[1] A. Kitaev, Anyons in an exactly solved model and beyond, *Annals of Physics* **321**, 2 (2006).

[2] C. Nayak, S. H. Simon, A. Stern, M. Freedman, and S. D. Sarma, Non-Abelian anyons and topological quantum computation, *Reviews of Modern Physics* **80**, 1083 (2008).

[3] G. Jackeli and G. Khaliullin, Mott insulators in the strong spin-orbit coupling limit: from Heisenberg to a quantum compass and Kitaev models, *Physical review letters* **102**, 017205 (2009).

[4] J. Chaloupka, G. Jackeli, and G. Khaliullin, Kitaev-Heisenberg model on a honeycomb lattice: possible exotic phases in iridium oxides A_2IrO_3 , *Physical review letters* **105**, 027204 (2010).

[5] F. Bahrami, W. Lafargue-Dit-Hauret, O. I. Lebedev, R. Movshovich, H.-Y. Yang, D. Broido, X. Rocquefelte, and F. Tafti, Thermodynamic evidence of proximity to a kitaev spin liquid in $\text{Ag}_3\text{LiIr}_2\text{O}_6$, *Physical Review Letters* **123**, 237203 (2019).

[6] K. Kitagawa, T. Takayama, Y. Matsumoto, A. Kato, R. Takano, Y. Kishimoto, S. Bette, R. Dinnebier, G. Jackeli, and H. Takagi, A spin-orbital-entangled quantum liquid on a honeycomb lattice, *Nature* **554**, 341 (2018).

[7] F. Bahrami, E. M. Kenney, C. Wang, A. Berlie, O. I. Lebedev, M. J. Graf, and F. Tafti, Effect of structural disorder on the kitaev magnet $\text{ag}_3\text{liir}_2\text{o}_6$, *Phys. Rev. B* **103**, 094427 (2021).

[8] Y. Li and R. Valentí, Role of disorder in electronic and magnetic properties of $\text{ag}_3\text{liir}_2\text{o}_6$, *Phys. Rev. B* **105**, 115123 (2022).

[9] K. Plumb, J. Clancy, L. Sandilands, V. V. Shankar, Y. Hu, K. Burch, H.-Y. Kee, and Y.-J. Kim, α - RuCl_3 : A spin-orbit assisted mott insulator on a honeycomb lattice, *Physical Review B* **90**, 041112 (2014).

[10] A. Banerjee, C. Bridges, J.-Q. Yan, A. Aczel, L. Li, M. Stone, G. Granroth, M. Lumsden, Y. Yiu, J. Knolle, *et al.*, Proximate kitaev quantum spin liquid behaviour in a honeycomb magnet, *Nature materials* **15**, 733 (2016).

[11] Y. Kasahara, T. Ohnishi, Y. Mizukami, O. Tanaka, S. Ma, K. Sugii, N. Kurita, H. Tanaka, J. Nasu, Y. Motome, T. Shibauchi, and Y. Matsuda, Majorana quantization and half-integer thermal quantum hall effect in a kitaev spin liquid, *Nature* **559**, 227 (2018).

[12] P. Czajka, T. Gao, M. Hirschberger, P. Lampen-Kelley, A. Banerjee, J. Yan, D. G. Mandrus, S. E. Nagler, and N. Ong, Oscillations of the thermal conductivity in the spin-liquid state of α - RuCl_3 , *Nature Physics* **17**, 915 (2021).

[13] J. Bruin, R. Claus, Y. Matsumoto, J. Nuss, S. Laha, B. Lotsch, N. Kurita, H. Tanaka, and H. Takagi, Origin of oscillatory structures in the magnetothermal conductivity of the putative kitaev magnet α - RuCl_3 , *arXiv preprint arXiv:2205.15839* (2022).

[14] J. Bruin, R. Claus, Y. Matsumoto, N. Kurita, H. Tanaka, and H. Takagi, Robustness of the thermal hall effect close to half-quantization in α - RuCl_3 , *Nature Physics* **18**, 401 (2022).

[15] Y. Kasahara, S. Suetsugu, T. Asaba, S. Kasahara, T. Shibauchi, N. Kurita, H. Tanaka, and Y. Matsuda, Quantized and unquantized thermal hall conductance of kitaev spin-liquid candidate α - RuCl_3 , *arXiv preprint arXiv:2202.11947* (2022).

[16] H. Liu and G. Khaliullin, Pseudospin exchange interactions in d^7 cobalt compounds: possible realization of the Kitaev model, *Physical Review B* **97**, 014407 (2018).

[17] R. Sano, Y. Kato, and Y. Motome, Kitaev-heisenberg hamiltonian for high-spin d^7 mott insulators, *Phys. Rev. B* **97**, 014408 (2018).

[18] H. Liu, Towards kitaev spin liquid in 3d transition metal compounds, *International Journal of Modern Physics B* **35**, 2130006 (2021).

[19] L. Viciu, Q. Huang, E. Morosan, H. Zandbergen, N. Greenbaum, T. McQueen, and R. Cava, Structure and basic magnetic properties of the honeycomb lattice compounds $\text{Na}_2\text{Co}_2\text{TeO}_6$ and $\text{Na}_3\text{Co}_2\text{SbO}_6$, *Journal of Solid State Chemistry* **180**, 1060 (2007).

[20] S. M. Winter, Magnetic couplings in edge-sharing d^7 compounds, *arXiv preprint arXiv:2204.09856* (2022).

[21] C. Kim, J. Jeong, G. Lin, P. Park, T. Masuda, S. Asai, S. Itoh, H.-S. Kim, H. Zhou, J. Ma, *et al.*, Antiferromagnetic kitaev interaction in $J_{eff}=1/2$ cobalt honeycomb materials $\text{Na}_3\text{Co}_2\text{SbO}_6$ and $\text{Na}_2\text{Co}_2\text{TeO}_6$, *Journal of Physics: Condensed Matter* **34**, 045802 (2021).

[22] G. Lin, J. Jeong, C. Kim, Y. Wang, Q. Huang, T. Masuda, S. Asai, S. Itoh, G. Günther, M. Russina, *et al.*, Field-induced quantum spin disordered state in spin-1/2 honeycomb magnet $\text{Na}_2\text{Co}_2\text{TeO}_6$, *Nature communications* **12**, 1 (2021).

[23] A. L. Sanders, R. A. Mole, J. Liu, A. J. Brown, D. Yu, C. D. Ling, and S. Rachel, Dominant kitaev interactions in the honeycomb materials $\text{Na}_3\text{Co}_2\text{SbO}_6$ and $\text{Na}_2\text{Co}_2\text{TeO}_6$, *Physical Review B* **106**, 014413 (2022).

[24] W. Yao, K. Iida, K. Kamazawa, and Y. Li, Excitations in the ordered and paramagnetic states of honeycomb magnet $\text{Na}_2\text{Co}_2\text{TeO}_6$, *Phys. Rev. Lett.* **129**, 147202 (2022).

[25] A. Bera, S. Yusuf, A. Kumar, and C. Ritter, Zigzag antiferromagnetic ground state with anisotropic correlation lengths in the quasi-two-dimensional honeycomb lattice compound $\text{Na}_2\text{Co}_2\text{TeO}_6$, *Physical Review B* **95**, 094424 (2017).

[26] X. Hong, M. Gillig, R. Hentrich, W. Yao, V. Kocsis, A. R. Witte, T. Schreiner, D. Baumann, N. Pérez, A. U. Wolter, *et al.*, Strongly scattered phonon heat transport of the candidate kitaev material $\text{Na}_2\text{Co}_2\text{TeO}_6$, *Physical Review B* **104**, 144426 (2021).

[27] G. Xiao, Z. Xia, Y. Song, and L. Xiao, Magnetic properties and phase diagram of quasi-two-dimensional $\text{Na}_2\text{Co}_2\text{TeO}_6$ single crystal under high magnetic field, *Journal of Physics: Condensed Matter* **34**, 075801 (2021).

[28] G. Lin, Q. Zhao, G. Li, M. Shu, Y. Ma, J. Jiao, Q. Huang, J. Sheng, A. Kolesnikov, L. Li, *et al.*, Evidence for field induced quantum spin liquid behavior in a spin-1/2 honeycomb magnet, *Research Square* [<https://doi.org/10.21203/rs.3.rs-2034295/v1>] (2022).

[29] E. Lefrançois, M. Songvilay, J. Robert, G. Nataf, E. Jordan, L. Chaix, C. Colin, P. Lejay, A. Hadj-Azzem, R. Balalou, *et al.*, Magnetic properties of the honeycomb oxide $\text{Na}_2\text{Co}_2\text{TeO}_6$, *Physical Review B* **94**, 214416 (2016).

[30] R. D. Johnson, S. Williams, A. Haghighirad, J. Singleton, V. Zapf, P. Manuel, I. Mazin, Y. Li, H. O. Jeschke, R. Valentí, *et al.*, Monoclinic crystal structure of α - RuCl_3 and the zigzag antiferromagnetic ground state, *Physical Review B* **92**, 235119 (2015).

[31] M. Songvilay, J. Robert, S. Petit, J. Rodriguez-Rivera, W. Ratcliff, F. Damay, V. Balédent, M. Jiménez-Ruiz, P. Lejay, E. Pachoud, *et al.*, Kitaev interactions in the Co honeycomb antiferromagnets $\text{Na}_3\text{Co}_2\text{SbO}_6$ and $\text{Na}_2\text{Co}_2\text{TeO}_6$, *Physical Review B* **102**, 224429 (2020).

[32] A. M. Samarakoon, Q. Chen, H. Zhou, and V. O. Garlea, Static and dynamic magnetic properties of honeycomb lattice antiferromagnets $\text{Na}_2\text{M}_2\text{TeO}_6$, $\text{M} = \text{Co}$ and Ni , *Physical Review B* **104**, 184415 (2021).

[33] W. Chen, X. Li, Z. Hu, Z. Hu, L. Yue, R. Sutarto, F. He, K. Iida, K. Kamazawa, W. Yu, *et al.*, Spin-orbit phase behavior of $\text{Na}_2\text{Co}_2\text{TeO}_6$ at low temperatures, *Physical Review B* **103**, L180404 (2021).

[34] C. Lee, S. Lee, Y. Choi, Z. Jang, R. Kalaivanan, R. Sankar, and K.-Y. Choi, Multistage development of anisotropic magnetic correlations in the co-based honeycomb lattice $\text{Na}_2\text{Co}_2\text{TeO}_6$, *Physical Review B* **103**, 214447 (2021).

[35] W. Yao and Y. Li, Ferrimagnetism and anisotropic phase tunability by magnetic fields in $\text{Na}_2\text{Co}_2\text{TeO}_6$, *Physical Review B* **101**, 085120 (2020).

[36] S. Zhang, M. Lee, S. Lee, A. J. Woods, S. M. Thomas, R. Movshovich, E. Broska, Q. Huang, H. Zhou, and V. Zapf, Supplemental material of electronic and magnetic phase diagrams of kitaev quantum spin liquid candidate $\text{Na}_2\text{Co}_2\text{TeO}_6$, URL_will_be_inserted_by_publisher (2022).

[37] V. S. Zapf, M. Kenzelmann, F. Wolff-Fabris, F. Balakirev, and Y. Chen, Magnetically induced electric polarization in an organometallic magnet, *Phys. Rev. B* **82**, 060402 (2010).

[38] Y.-S. Chai, J.-Z. Cong, J.-C. He, D. Su, X.-X. Ding, J. Singleton, V. Zapf, and Y. Sun, Giant magnetostriction and nonsaturating electric polarization up to 60 t in the polar magnet $\text{CaBaco}_4\text{O}_7$, *Phys. Rev. B* **103**, 174433 (2021).

[39] R. Schönemann, S. Imajo, F. Weickert, J. Yan, D. G. Mandrus, Y. Takano, E. L. Broska, P. F. Rosa, S. E. Nagler, K. Kindo, *et al.*, Thermal and magnetoelastic properties of α - RuCl_3 in the field-induced low-temperature states, *Physical Review B* **102**, 214432 (2020).

[40] M. Jaime, C. Corvalán Moya, F. Weickert, V. Zapf, F. F. Balakirev, M. Wartenbe, P. F. Rosa, J. B. Betts, G. Rodriguez, S. A. Crooker, *et al.*, Fiber Bragg grating dilatometry in extreme magnetic field and cryogenic conditions, *Sensors* **17**, 2572 (2017).

[41] S. Mukherjee, G. Manna, P. Saha, S. Majumdar, and S. Giri, Ferroelectric order with a linear high-field magnetoelectric coupling in $\text{Na}_2\text{Co}_2\text{TeO}_6$: A proposed kitaev compound, *Physical Review Materials* **6**, 054407 (2022).

[42] M. Lee, J. Hwang, E. S. Choi, J. Ma, C. R. Dela Cruz, M. Zhu, X. Ke, Z. L. Dun, and H. D. Zhou, Series of phase transitions and multiferroicity in the quasi-two-dimensional spin- $\frac{1}{2}$ triangular-lattice antiferromagnet $\text{Ba}_3\text{CoNb}_2\text{O}_9$, *Phys. Rev. B* **89**, 104420 (2014).

[43] X. Mi, X. Wang, H. Gui, M. Pi, T. Zheng, K. Yang, Y. Gan, P. Wang, A. Li, A. Wang, *et al.*, Stacking faults in α - RuCl_3 revealed by local electric polarization, *Physical Review B* **103**, 174413 (2021).

[44] J.-C. Zheng, Y. Cui, T.-R. Li, K.-J. Ran, J. Wen, and W. Yu, Dielectric evidence for possible type-ii multiferroicity in α - RuCl_3 , *arXiv preprint arXiv:1801.08277* (2018).

[45] S. Bachus, D. A. Kaib, Y. Tokiwa, A. Jesche, V. Tsurkan, A. Loidl, S. M. Winter, A. A. Tsirlin, R. Valentí, and P. Gegenwart, Thermodynamic perspective on field-induced behavior of α - RuCl_3 , *Physical Review Letters* **125**, 097203 (2020).

[46] G. Xiao, Z. Xia, W. Zhang, X. Yue, S. Huang, X. Zhang, F. Yang, Y. Song, M. Wei, H. Deng, *et al.*, Crystal growth and the magnetic properties of $\text{Na}_2\text{Co}_2\text{TeO}_6$ with quasi-two-dimensional honeycomb lattice, *Crystal Growth & Design* **19**, 2658 (2019).

[47] M. Lee, E. S. Choi, X. Huang, J. Ma, C. R. Dela Cruz, M. Matsuda, W. Tian, Z. L. Dun, S. Dong, and H. D. Zhou, Magnetic phase diagram and multiferroicity of $\text{ba}_3\text{mn}_2\text{nb}_2\text{o}_9$: A spin- $\frac{5}{2}$ triangular lattice antiferromagnet with weak easy-axis anisotropy, *Phys. Rev. B* **90**, 224402 (2014).

[48] J. A. Sears, Y. Zhao, Z. Xu, J. W. Lynn, and Y.-J. Kim, Phase diagram of α - RuCl_3 in an in-plane magnetic field, *Physical Review B* **95**, 180411 (2017).

[49] Q. Huang, M. Lee, E. sang Choi, J. Ma, C. D. Cruz, and H. Zhou, Successive phase transitions and multiferroicity in deformed triangular-lattice antiferromagnets $\text{Ca}_3\text{MnNb}_2\text{O}_9$ ($\text{M} = \text{Co, Ni}$) with spatial anisotropy, *ECS Journal of Solid State Science and Technology* (2022).

[50] G.-W. Chern, Y. Sizuk, C. Price, and N. B. Perkins, Kitaev-heisenberg model in a magnetic field: order-by-disorder and commensurate-incommensurate transitions, *Physical Review B* **95**, 144427 (2017).

[51] L. Janssen, E. C. Andrade, and M. Vojta, Honeycomb-lattice heisenberg-kitaev model in a magnetic field: Spin canting, metamagnetism, and vortex crystals, *Phys. Rev. Lett.* **117**, 277202 (2016).

[52] L. Janssen and M. Vojta, Heisenberg-kitaev physics in magnetic fields, *Journal of Physics: Condensed Matter* **31**, 423002 (2019).

[53] N. Li, S. Guang, W. Chu, Q. Huang, J. Liu, K. Xia, X. Zhou, X. Yue, Y. Sun, Y. Wang, *et al.*, Sign switchable magnon thermal hall conductivity in an antiferromagnet, arXiv preprint arXiv:2201.11396 (2022).

[54] C. Balz, P. Lampen-Kelley, A. Banerjee, J. Yan, Z. Lu, X. Hu, S. M. Yadav, Y. Takano, Y. Liu, D. A. Tennant, M. D. Lumsden, D. Mandrus, and S. E. Nagler, Finite field regime for a quantum spin liquid in α -RuCl₃, *Phys. Rev. B* **100**, 060405 (2019).

[55] P. Lampen-Kelley, L. Janssen, E. Andrade, S. Rachel, J.-Q. Yan, C. Balz, D. Mandrus, S. Nagler, and M. Vojta, Field-induced intermediate phase in α -RuCl₃: Non-coplanar order, phase diagram, and proximate spin liquid, arXiv preprint arXiv:1807.06192 (2018).

[56] R. G. Pereira and R. Egger, Electrical access to ising anyons in kitaev spin liquids, *Phys. Rev. Lett.* **125**, 227202 (2020).

[57] L. D. Landau, *Zh. Eksp. Teor. Fiz.* **7**, 627 (1937), or, "On phase transitions II", by L. D. Landau, in "Collected Works of L. D. Landau", Gordon and Breach, N. Y., 1965).

[58] S. K. Yip, T. Li, and P. Kumar, Thermodynamic considerations and the phase diagram of superconducting up₃, *Phys. Rev. B* **43**, 2742 (1991).

Supplemental Material of “Electronic and magnetic phase diagrams of Kitaev quantum spin liquid candidate $\text{Na}_2\text{Co}_2\text{TeO}_6$ ”

Shengzhi Zhang,* Vivien S. Zapf,[†] and Minseong Lee[‡]

National High Magnetic Field Laboratory, Los Alamos National Laboratory, Los Alamos, NM 87545, USA.

Sangyun Lee, Andrew J. Woods, Sean M. Thomas, and Roman Movshovich
MPA-Q, Los Alamos National Laboratory, Los Alamos, New Mexico 87545, USA.

Eric Brosha
Los Alamos National Laboratory, Los Alamos, NM 87545, USA.

Qing Huang and Haidong Zhou

Department of Physics, University of Tennessee, Knoxville, TN 37996, USA.

(Dated: December 8, 2022)

EXPERIMENTAL CONFIGURATIONS

In this section we illustrate the experimental setup of the magnetocaloric effect and magnetostriction measurements.

Shown in the left-hand-side of Fig. S1 is a schematic drawing of the wiring configuration of magnetocaloric effect. As-grown $\text{Na}_2\text{Co}_2\text{TeO}_6$ single crystal was deposited by a 10 nm AuGe thin film on the ab-plane and two gold contact pads were deposited on the thin film, leaving a stripe exposed. Twisted pair wires were attached to the contact pads using silver paint. Then a standard four-probe resistance measurement was carried out in the 65 T Pulsed Field facility whose set-up is illustrated in the right-hand-side of Fig. S1. A sourcing voltage (V_{source}) is supplied from the red pitaya and converted into current (I_{source}) by Stanford Research System (SRS) CS580 voltage-controlled current source. The induced voltage from the sample is amplified by a SRS SR560 voltage pre-amplifier ($V_s \rightarrow PV_s$) before measured in the red pitaya. Magnetic field was applied within the plane so that heating from eddy current did not happen.

Shown in Fig. S2 is an illustration of the crystal attached to the optical fiber in the magnetostriction measurement using Fiber Bragg Grating technique. Single crystalline $\text{Na}_2\text{Co}_2\text{TeO}_6$ was attached to the 2 mm grates using Pattex ultra gel superglue along either a - or a^* -axis. The edge of the sample is much longer than the length of the grates to ensure a full coverage. As demonstrated, the sample is thinner than the fiber so a certain amount of superglue was needed to ensure a secure bonding which may cause extra strain on the sample.

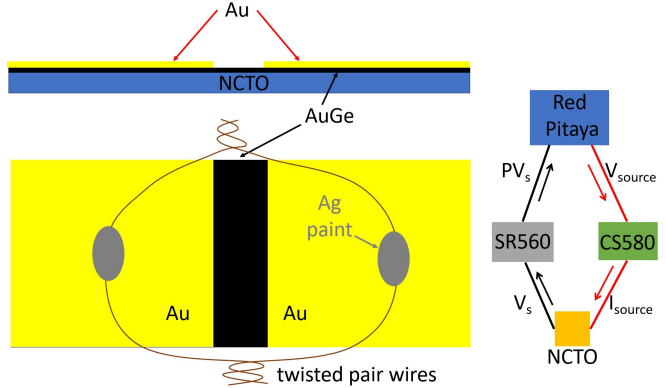


FIG. S1. Top and bottom of the left panel respectively show the side view and top view of the magnetocaloric effect measurement wiring configuration. The right hand side illustrates the standard four-point resistance measurement set-up. V_{source} , I_{source} are the sourcing voltage from the red pitaya and the converted current applied to the sample, respectively. V_s is the induced voltage in the sample, P is the amplification of the pre-amplifier (SR560).

COMPLETE DATA SETS

Magnetization

Fig. S3 (a)-(d) are the complete data sets of dc magnetization measurements from which Fig. 2 and Fig. 3 in the main text are selected. The hysteresis behavior with $H \parallel a^*$ is more clearly shown in Fig. S3 (d). Panel (e) and (f) are the magnetic field dependent ac susceptibility illustrating the absence of frequency dependence. A pronounced hysteresis loop is again observed when $H \parallel a^*$.

The c-axis magnetic susceptibility data are displayed in Fig. S4 (a) and (b). Similarly to the in-plane measurements presented in the main text, the antiferromagnetic transition at $T_N \approx 27$ K as well as the spin canting at $T_F \approx 15$ K are both observed. Observation of

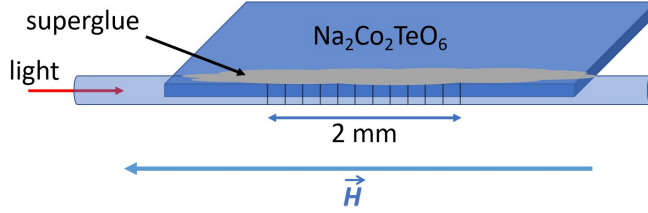


FIG. S2. A cartoon picture illustrating the configuration of the FBG magnetostriiction measurement. The thick rod and the set of vertical short lines represent the fiber and the Bragg grating, respectively. The grey amorphous shaped area represents the superglue. Magnetic field \mathbf{H} is applied along the fiber.

T_F is consistent with the scenario in which the spins are slightly canted towards c-axis. On the other hand, observation of T_N along c-axis suggests that this antiferromagnetic transition is three dimensional, in line with neutron scattering results [1]. However, it shows up as a sharp *increase* in magnetic susceptibility, drastically different from the in-plane behavior. With increasing magnetic field, both T_N and T_F increase slightly until 2 T above which they diminish. In addition to the critical temperatures observed in ab-plane, a broad peak is observed in the magnetic susceptibility at T_P (panel (a)) which splits into two peaks (T_{P1} and T_{P2}) at higher fields (panel (b)). T_{P2} gets suppressed by increasing magnetic field whereas T_{P2} remains largely constant even at 14 T. At even lower temperatures, an upturn appears at T_U which is quickly suppressed by very small magnetic field. Fig. S4 (d) shows the magnetic moment as a function of magnetic field up to 60 T. From their first derivatives, we can extract two critical fields defined by the major peak (inflection point H_I) and a second peak in the first derivative (H_P).

The c-axis temperature-field ($T - H$) phase diagram is plotted in Fig. S5. Similar to the in plane phase diagram Fig. 1 in main text, phase boundaries with little temperature dependence are observed (H_I , H_P). More data points are needed to complete this phase diagram.

Polarization

Electrical polarization along a^* -axis as a function of magnetic field along a -axis at 15.2 K is plotted in Fig. S6. Due to the ultra-fast field ramping rate of $\sim 10,000$ T/s, the polarization signal was expected to be large enough to be observed as the peak height of the magnetoelectric current is proportional to this rate. However, no pronounced feature is observed. The peak at 0.3 T is likely from extrinsic origins such as the vibration of the magnet at the beginning of the pulse due to the gigantic amount of current dumped into it. As will be illustrated next, a linear magnetoelectric coupling is expected for the triple-

Q structure. Therefore, the absence of such signatures from the positive and negative field sweeps in Fig. S6 suggests the triple-Q structure is not supported by our polarization measurement results. The inset of Fig. S6 depicts the same measurement at 4 K. It is clear that it is also featureless. On the other hand, the temperature dependent electrical polarization of a polycrystal at zero field also did not yield any noticeable features at the critical temperatures as illustrated in panel (b), which is in contrast to the electric polarization observed at 75 K [2].

Now we discuss a symmetry analysis showing a linear magnetoelectric coupling in the triple-Q scenario. With the triple-Q scenario, there exists a spontaneous toroidal moment whose order parameter \vec{t} is defined as

$$\vec{t} = \sum_n (\vec{r}_n \times \vec{S}_n), \quad (S1)$$

where \vec{S}_n and \vec{r}_n are n th spin and the vector from the center of a toroidal moment to the n th spin, respectively. \vec{t} is odd both under spatial inversion symmetry and time-reversal symmetry, which allows the following form of the free energy [3],

$$F(\mathbf{E}, \mathbf{H}) = F_0 - \frac{\varepsilon_{ij} E_i E_j}{8\pi} - \frac{\mu_{ij} H_i H_j}{8\pi} - \alpha_{ij} E_i H_j + \dots, \quad (S2)$$

where ε_{ij} , μ_{ij} , and α_{ij} are the dielectric permittivity, the magnetic permeability and the magnetoelectric tensor, respectively. Therefore, we expect the linearly increasing electric polarization as a function of the external magnetic field as follows.

$$P_i = \left(\frac{\varepsilon_{ij} - \delta_{ij}}{4\pi} \right) E_j + \alpha_{ij} H_j \quad (S3)$$

In this study, we measured the electric polarization as a function of magnetic field (H_j) without external electric field (E_i). That no electric polarization was observed in our experiments therefore strongly negates the triple-Q spin structure. Although S. Mukherjee *et al.*, [2] has observed an electric polarization in the title compound, it seems not directly correlated with magnetic ordering due to the large separation between magnetic ordering temperature and onset temperature of electric polarization.

Dielectric constant

The temperature dependent dielectric constant data measured at magnetic fields up to 14 T are shown in Fig. S7 (a) with magnetic field applied along a^* -axis and electric field along a -axis. Three weak humps at T_I through T_{III} are observed as indicated by the dotted lines. These hump features are better observed in the dissipation as pronounced peaks. Therefore, we show in Fig. S7 (b) the frequency dependent dissipation measured at $H = 7$ T. This is a good representation of all

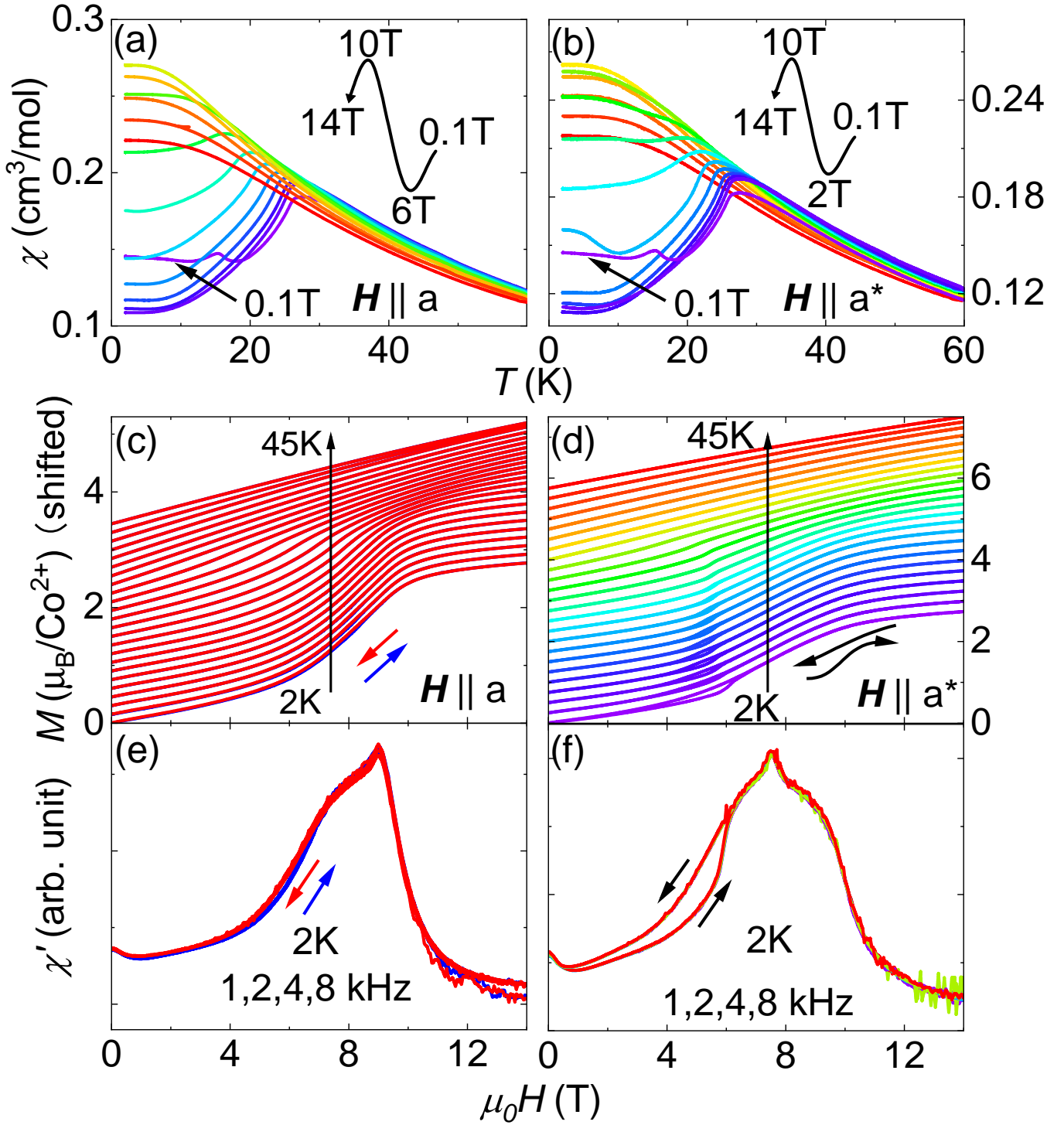


FIG. S3. (a),(b) Complete data set of magnetic susceptibility as a function of temperature for $H \parallel a$ and a^* , respectively. The S-shaped curves labeled with field strength illustrate the evolution of low temperature magnetic susceptibility with magnetic field. (c),(d) Complete data set of magnetization as a function of magnetic field for $H \parallel a$ and a^* , respectively. Curves are shifted from 2 K data for clarity.

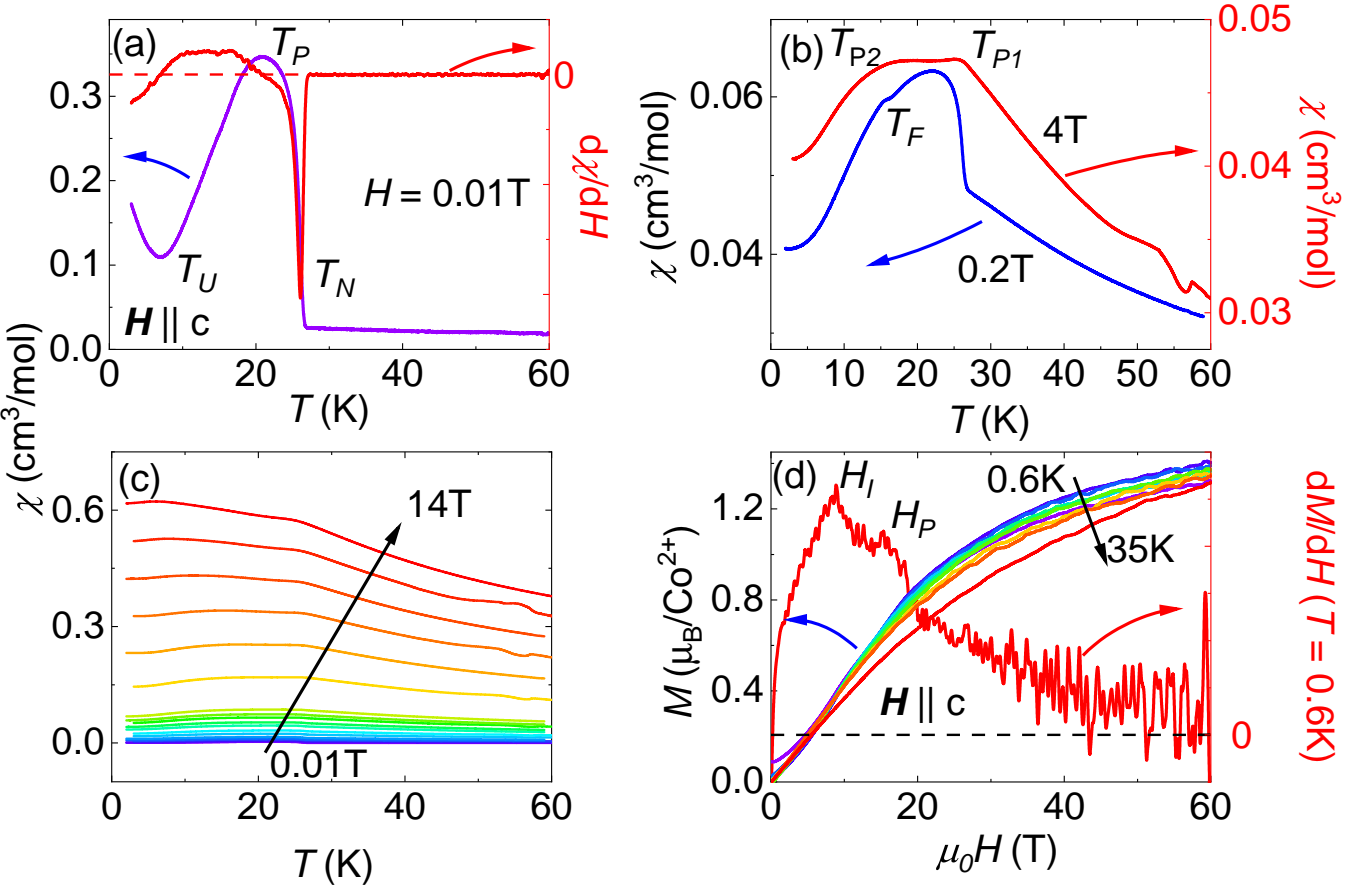


FIG. S4. $\mathbf{H} \parallel \mathbf{c}$ (a),(b) Magnetic susceptibility (χ) as a function of temperature taken at 0.01 T, 0.2 T and 2 T to show the critical temperatures in Fig. S5. (c) A complete data set of temperature dependent χ from 0.01 T to 14 T. (d) Magnetic moment as a function of applied magnetic field in a temperature range of 0.6 K to 35 K. This is measured in a 65 T pulsed field facility. The right axis is the derivative dM/dH at 0.6 K. Critical fields used in Fig. S5 are also labeled.

magnetic fields because the features showed no dependence on magnetic field strength as illustrated in panel (a). As indicated by the dotted lines in panel (b), $T_{I,II,III}$ all increase with increasing frequency from 50 kHz to 2 MHz. By plotting the Arrhenius plot for all three features (Figs. S7(c) - (e)), the activation energies of T_I to T_{III} features are extracted to be 11.27(1.9) meV, 35.68(1.2) meV, and 64.06(3.1) meV, respectively. In addition to their lacking magnetic field dependence, it should also be pointed out that none of $T_{I,II,III}$ matches the magnetic transitions plotted in Fig. 1 in main text, indicating that they are not associated with any magnetic orderings. Therefore, these features likely come from the freezing of Na⁺ positions as temperature decreases.

The complete data set of dielectric constant as a function of magnetic field are plotted in Figs. S8, S9, and S10 for $H \parallel a$, $H \parallel a^*$ and $H \parallel c$, respectively. The hysteretic behavior of H_1 is more clearly shown in Figs. S8 and S9. Note that in Fig. S10, no pronounced feature is observed up to 14 T.

Thermal expansion

The complete data set of thermal expansion as a function of temperature and magnetostriction are shown in Figs. S11 and S12, respectively. Temperature dependent thermal expansion exhibits a non-monotonic magnetic field dependence with 6 - 7 T as the turning point, roughly consistent with the H_1 phase transition. The magnetostriction along a -axis shows a monotonic temperature dependence. The sudden jump between the obviously two sets of curves occurs at T_N . On the other hand, the a^* -axis magnetostriction shows a non-monotonic temperature dependence with T_N as the turning point.

Magnetocaloric effect

The complete data set of magnetocaloric effect measurements is shown in Fig. S13. For clarity, only the up sweep field is plotted.

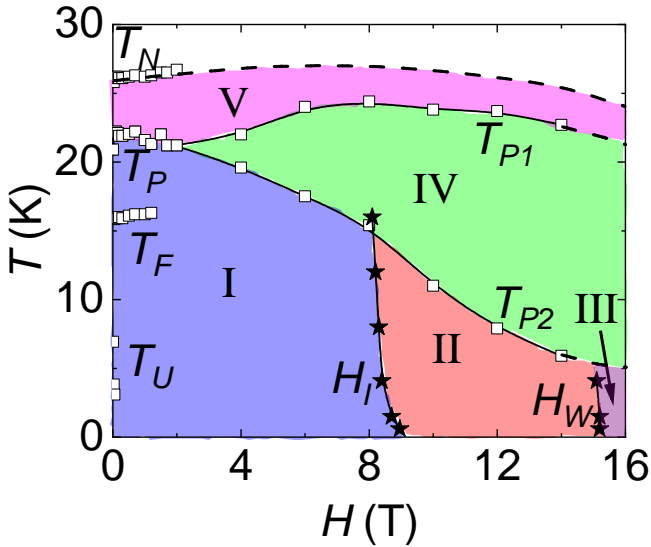


FIG. S5. $\mathbf{H} \parallel \mathbf{c}$ temperature-field (\mathbf{T} - \mathbf{H}) phase diagram constructed from Fig. S4. The empty squares are from temperature sweeps and the solid stars are from magnetic field sweeps. The phase regions are labeled from I-V. Add $\mathbf{H} \perp \mathbf{c}$ to phase diagram somewhere? can make the \mathbf{T} axis go to 35 K..

* shengzhi@lanl.gov

† vzapf@lanl.gov

‡ ml10k@lanl.gov

- [1] W. Chen, X. Li, Z. Hu, Z. Hu, L. Yue, R. Sutarto, F. He, K. Iida, K. Kamazawa, W. Yu, *et al.*, Spin-orbit phase behavior of $\text{Na}_2\text{Co}_2\text{TeO}_6$ at low temperatures, *Physical Review B* **103**, L180404 (2021).
- [2] S. Mukherjee, G. Manna, P. Saha, S. Majumdar, and S. Giri, Ferroelectric order with a linear high-field magnetoelectric coupling in $\text{Na}_2\text{Co}_2\text{TeO}_6$: A proposed kitaev compound, *Physical Review Materials* **6**, 054407 (2022).
- [3] N. A. Spaldin, M. Fiebig, and M. Mostovoy, The toroidal moment in condensed-matter physics and its relation to the magnetoelectric effect, *Journal of Physics: Condensed Matter* **20**, 434203 (2008).

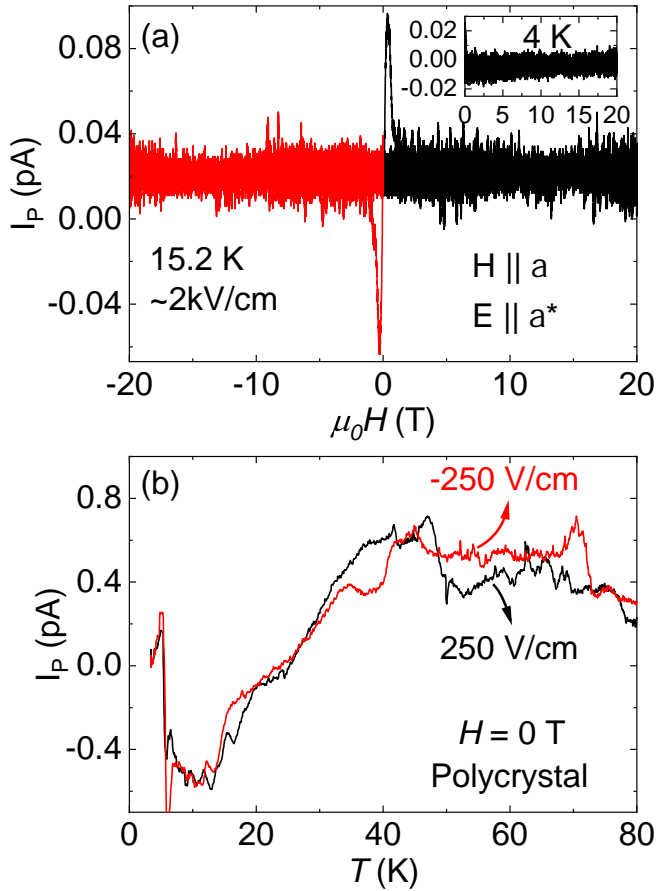


FIG. S6. (a) Electrical polarization along a^* -axis measured at 15.2 K with $H \parallel a$ for both positive and negative field sweeps. The polling voltage is about 2 kV/cm. Inset depicts the positive sweep of the same measurement configuration at 4 K. (b) Electrical polarization as a function of temperature of a polycrystalline sample measured at 0 T and with a 250 V/cm polling voltage. The black and red lines are positively and negatively polled, respectively.

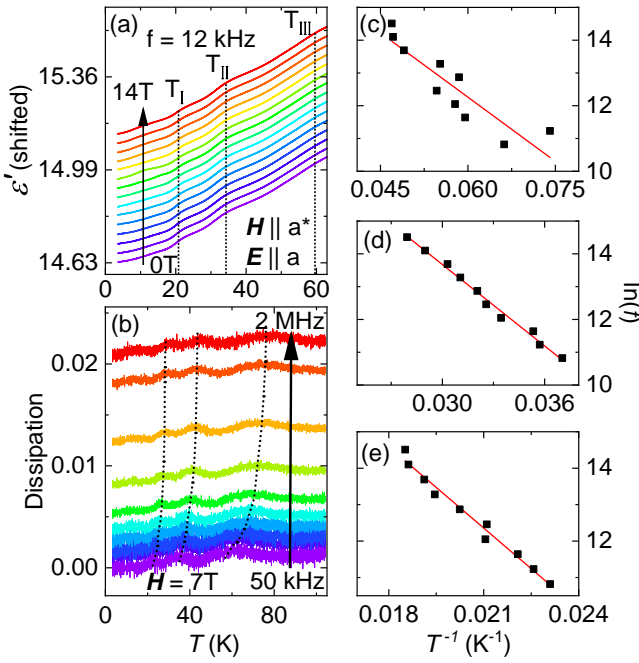


FIG. S7. (a) Dielectric constant (ϵ') as a function of temperature under various magnetic field up to 14 T when magnetic field is applied along a^* -axis and electric field along a -axis. The labels T_{I} , T_{II} , and T_{III} indicate the temperatures at which three humps are observed. The dotted lines are guide to the eyes showing $T_{\text{I,II,III}}$ are independent of magnetic field. The other curves are shifted from $H = 0$ T curve for clarity. (b) Dissipation as a function of temperature measured with various frequencies. The dashed lines are guide to the eyes showing $T_{1,2,3}$ are frequency dependent. (c) - (f) $\ln(f)$ of each curve as a function of the locations of hump 1 to hump 3 in terms of T^{-1} , respectively. The solid red lines are fittings to the Arrhenius expression $\ln(f) = \ln(A) - \frac{E_a}{k_B} \frac{1}{T}$.

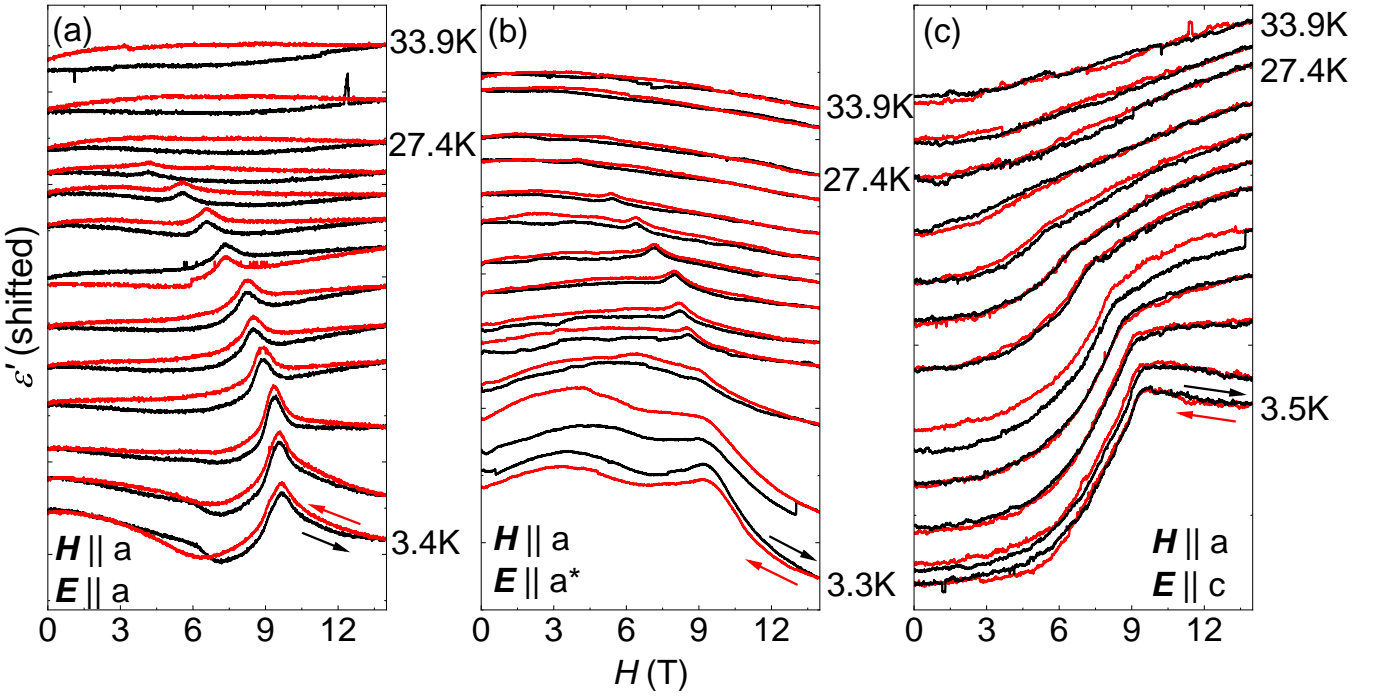


FIG. S8. Dielectric constant as a function of magnetic field (H) when $H \parallel a$ -axis taken at various temperatures. The electric field is applied along (a) a -, (b) a^* -, and (c) c -axes, respectively.

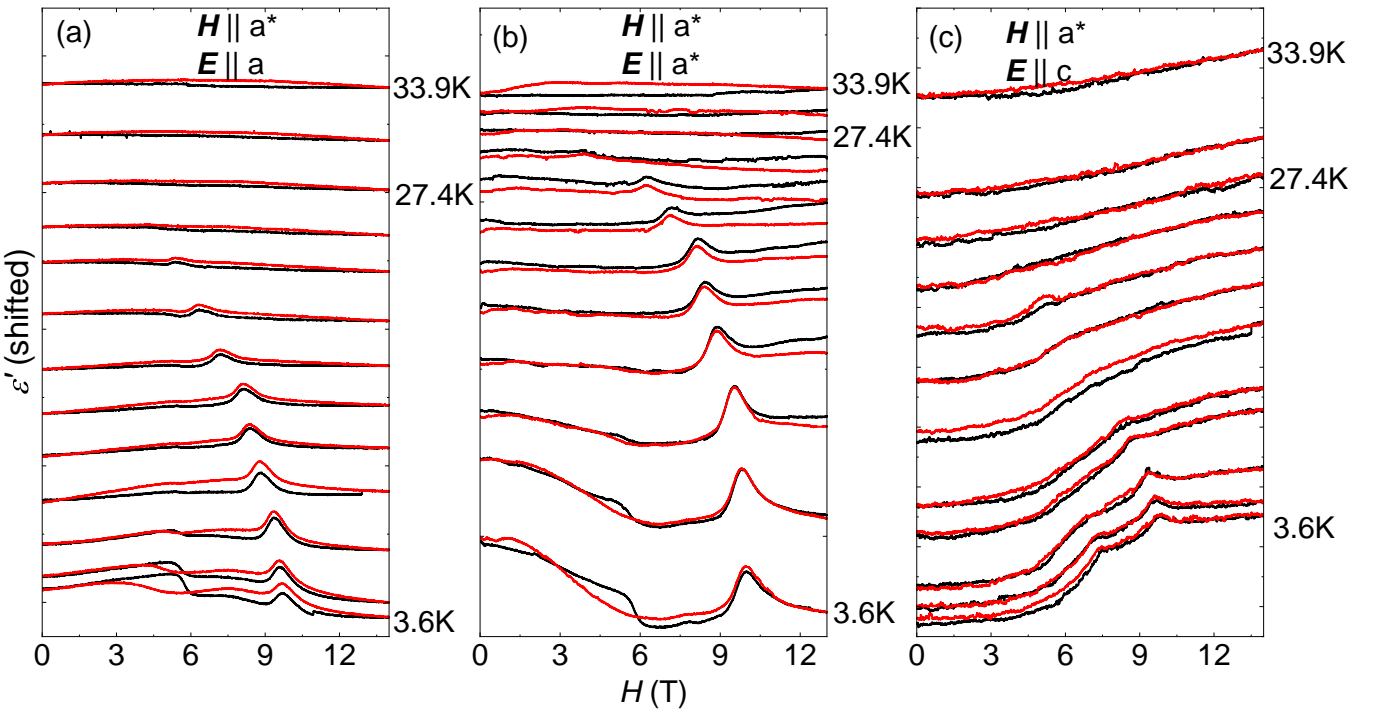


FIG. S9. Dielectric constant as a function of magnetic field (H) when $H \parallel a^*$ -axis taken at various temperatures. The electric field is applied along (a) a -, (b) a^* -, and (c) c -axes, respectively.

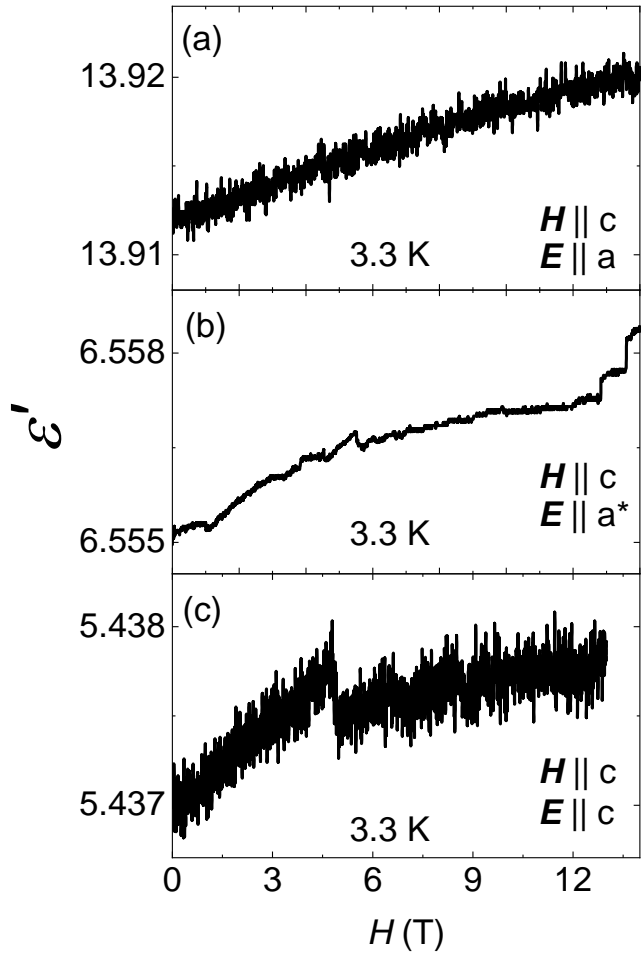


FIG. S10. Dielectric constant as a function of magnetic field (H) when $H \parallel c$ -axis taken at 3.3 K. The electric field is applied along (a) a -, (b) a^* -, and (c) c -axes, respectively.

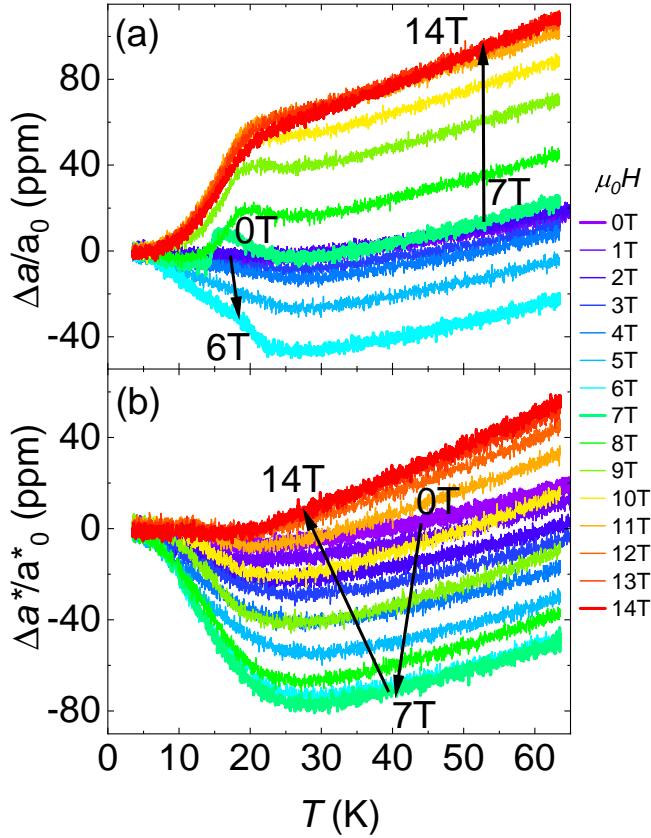


FIG. S11. Complete data set of thermal expansion as a function of temperature measured at various magnetic fields. The arrows illustrate the evolution of the curves with increasing magnetic field.

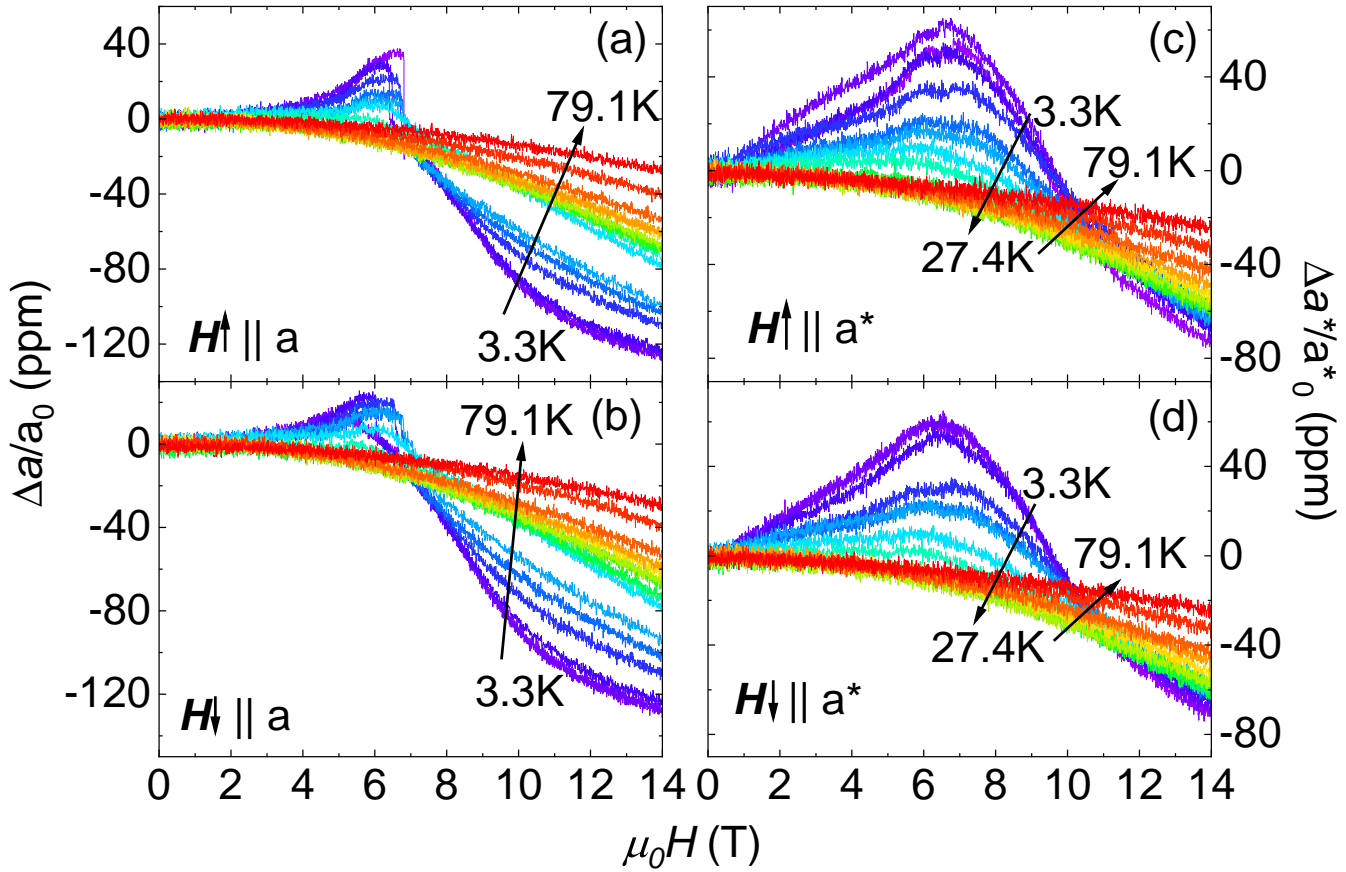


FIG. S12. Complete data set of magnetostriction measured at various temperatures. The arrows illustrate the evolution of the curves with increasing temperature.

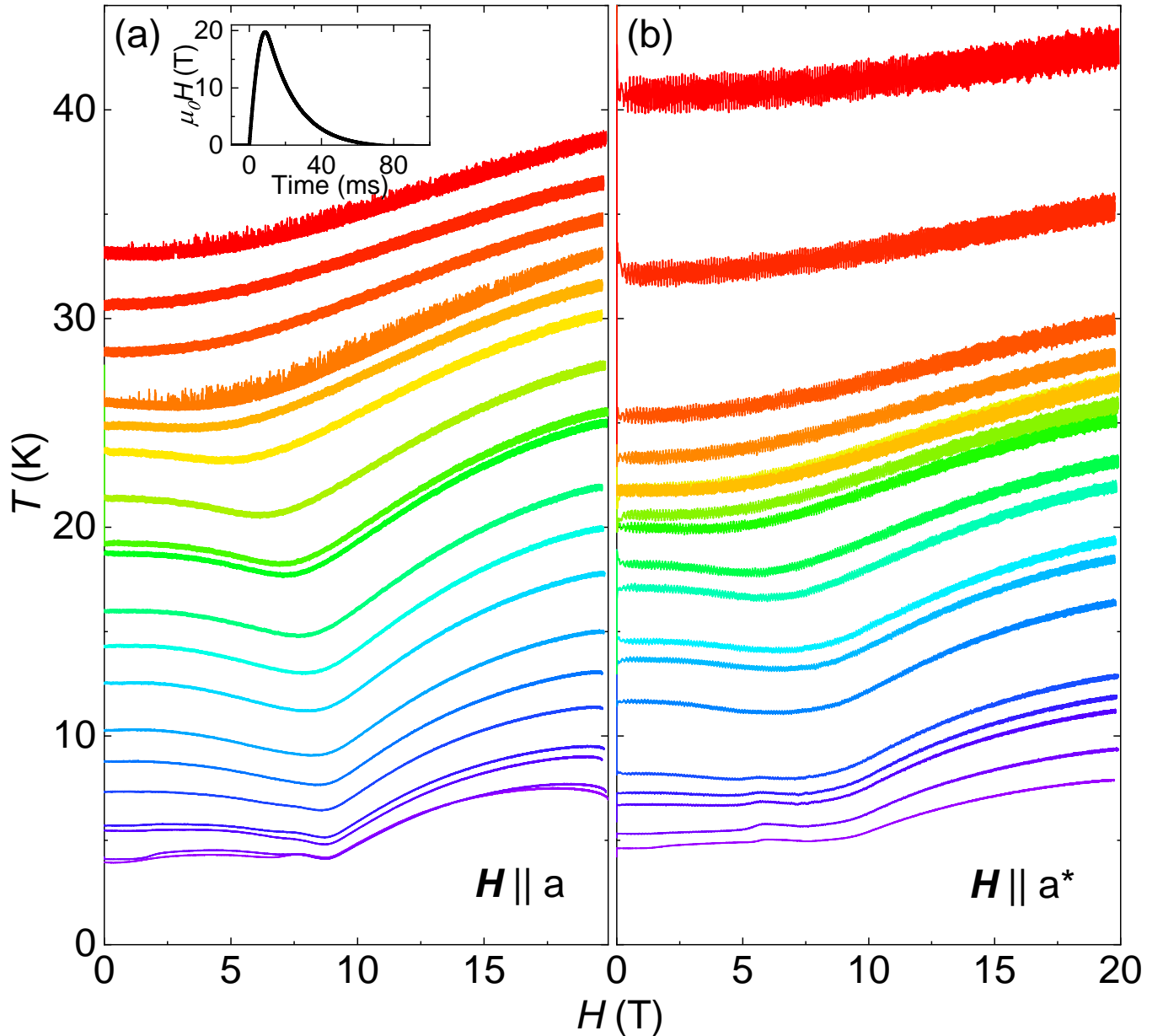


FIG. S13. Complete data set of sample temperature as a function of magnetic field from magnetocaloric effect measurements when (a) $H \parallel a$ -axis and (b) $H \parallel a^*$ -axis. The inset of (a) illustrates the magnetic field as a function of time during one pulse using the 65 T pulsed magnet.